



Thermal Effects on Tension Softening Response and Fracture Characteristics of Quartz-Diorite

You Wu¹ · Tubing Yin¹ · Dengdeng Zhuang¹ · Yongjun Chen¹ · Zheng Yang¹

Received: 23 November 2022 / Accepted: 9 April 2023 / Published online: 31 May 2023
© The Author(s), under exclusive licence to Springer-Verlag GmbH Austria, part of Springer Nature 2023

Abstract

Identifying the thermal effects on the tension softening curve is of great significance for understanding the fracture characteristics of rock specimens after thermal treatments and provides the experimental basis for the application of the cohesive zone model in high-temperature rock engineering. In this paper, three-point bend fracture tests were carried out on the quartz-diorite rock after different high temperatures. The digital image correlation technique was applied to access the crack propagation behaviours and the crack opening profiles under different loading stages. The initial fracture toughness and the cohesive stress-based fracture criterion were used to calculate the tension-softening curves. The results indicated that the shape of the tension-softening curve is not affected by the heat treatment, and the cohesive stress varies linearly with the crack opening displacement. The obtained tension softening curves were employed to predict the fracture characteristics under different temperatures and specimen depths. For the specimen with a depth of 45 mm, the increase in temperature can lead to an increase in the crack length and the fracture process zone length at the same load level under the premise that the crack has initiated from the pre-fabricated crack tip. The fracture toughness and fracture process zone length at the peak load are size-dependent. For specimens at 25 °C, the fracture toughness at peak load increases with specimen size. However, a contrary tendency can be observed for specimens at 200, 400, and 600 °C. The fracture process zone length at peak load for all temperature specimens was increased by increasing the specimen depth. This study sheds light on the determination of the tension-softening curve and its relation to the fracture behaviours of heat-treated rock specimens.

Highlights

- Tension softening curves of thermally treated quartz-diorite are determined based on the analytical approach.
- Effect of high temperature on the tension softening curves of quartz-diorite is investigated.
- Effect of high temperature on the development of the crack resistance curve and fracture process zone length is analyzed.
- Size effect on the fracture toughness and fracture process zone at peak load is revealed.

Keywords Cohesive zone model · Tension softening curve · High temperature · Fracture toughness · Fracture process zone

1 Introduction

The numerical simulation method coupled with the stress–strain failure criteria is a common approach to assessing the damage and failure of rock engineering structures.

However, rock is abundant in pore spaces, joint planes, and flaws. The failure process of the rock body is essentially linked to the initiation, propagation, and coalescence of cracks. The stress–strain failure criteria account for the failure of the complete rock matrix at ultimate conditions but fail to consider the stress discontinuities and singularities around the defects on the micro-scale. As a consequence, the researchers have considered incorporating the cohesive zone model (CZM) (Hillerborg et al. 1976) into the numerical

✉ Tubing Yin
tubing_yin@mail.csu.edu.cn

¹ School of Resources and Safety Engineering, Central South University, Changsha 410083, China

approaches to eliminate the weaknesses. It was shown that by meshing the specimen with the triangular elements and applying the zero-thickness cohesive elements among the triangular elements, the detailed fracture and fragmentation process of rock specimens could be well presented (Wu et al. 2018b, 2019).

The determination of the cohesive law might be one of the critical issues for numerical modeling with CZM. Different tension softening laws, such as triangular, exponential, trapezoidal, perfectly plastic, and linear/polynomial, have been used to predict the failure of various materials (Hallett and Harper 2015). For rock-like materials, such as concrete, the literature (Reinhardt et al. 1986; Guinea et al. 1994; Lee et al. 2008; Zhang et al. 2010; Chen and Su 2013) indicates that the degradation of cohesive stress follows the exponential or the bilinear law, and the shape of the softening function is highly related to the composition of the concrete. Whereas, a review of the literature (Wu et al. 2018b, 2019; Rasmussen et al. 2018; Ye et al. 2021; Wu et al. 2021; Jiao et al. 2022; Gao et al. 2022) demonstrates that the form of the tension softening relation has not received enough attention from the researchers, and the linear tension softening law was usually used in numerical works for rock materials. Since the numerical results are highly sensitive to the shape of tension-softening curves (Shet and Chandra 2004), using the pre-established equation in the numerical simulations may produce inaccurate results. It is necessary to investigate the form of softening function of rock materials.

In deep mining, geothermal resource exploitation, and tunneling engineering, the effect of temperature on the physio-mechanical properties of rock is worthy of full consideration. Previous studies demonstrated that the thermal treatment could seriously affect the rock's mechanical parameters, such as compressive strength (Liu and Xu 2015; Yang et al. 2017; Chen et al. 2021; Yin et al. 2021; Sciarretta et al. 2021; Zhang et al. 2022a), tensile strength (Yin et al. 2015, 2022; Sirdesai et al. 2017; Mardoukhi et al. 2017; Xu et al. 2020), and fracture toughness (Meredith and Atkinson 1985; Nasser et al. 2007; Feng et al. 2017; Miao et al. 2020; Wu et al. 2022b). This is to say that the shape of the tension-softening relation and corresponding controlling parameters might change owing to thermal treatment.

Furthermore, when the tension-softening relation of the specimen is known, it was shown that the fracture behaviours of the rock and rock-like materials could be well understood (Reinhardt and Xu 1999; Mai 2002; Wu et al. 2014; Wang et al. 2019; Dong et al. 2019, 2021; Lin et al. 2020). Thus, it is necessary to examine whether the tension-softening relation can be used to describe the fracture behaviours of the rock materials after heat treatment as well.

It should be noticed that it remains a challenge to directly measure the tension softening curves in the laboratory test. The direct method requires testing the complete tensile

stress–strain curves of rock samples. Nevertheless, in the rock direct tension test, it is not easy to get good control when the strain is beyond the peak strain, and usually, no stable post-peak stress–strain relation can be obtained (Yang et al. 2015; Cen et al. 2020; Zhu et al. 2022b). The inverse analysis approach provides an alternative approach to determining the tension softening law, and its effectiveness has been validated in numerous studies (Ulfkjaer et al. 1995; Abdalla and Karihaloo 2004; Slowik et al. 2006; Kwon et al. 2008; Zhang et al. 2010; Chen et al. 2013; Murthy et al. 2013; Hu and Fan 2019; Li et al. 2021; Tang et al. 2022).

The paper is structured as follows. In Sect. 2, the fracture test procedures, including specimen preparation, loading procedures, digital image correlation (DIC) setup, load (P)-crack mouth opening displacement (CMOD) curves, and fracture characteristics monitored by the DIC technique were presented. The theoretical background of the inverse analysis method and the determination of the fracture parameters were introduced in Sect. 3. Section 4 shows the tension-softening curves of the specimen after different thermal treatments, and the effectiveness of the tension-softening curves has been verified. The further fracture process analyses, completed based on the tension softening results, were conducted in Sect. 5. Finally, the conclusions of the text were drawn in Sect. 6. It will be shown that the temperature has a significant influence on the tension softening curve parameters and the fracture process of rock specimens.

2 Laboratory Experiments and Results

2.1 Specimen Preparation

The material used herein is quartz-diorite, collected from the Zhangzhou area of Fujian province, China. The rock material has a density of 2.780 g/cm³ and is considered homogeneous in the macro aspect. The main components of the rock are plagioclase (68%), quartz (18%), biotite (7%), hornblende (5%), Pyroxene (1%), and other opaque minerals (1%) (Wu et al. 2022c). The lithofacies observation results of the quartz-diorite can be seen in Fig. 1. Several beam specimens with depth $D = 45$ mm, thickness $B = 25$ mm, and length $L = 189$ mm were cut from a whole rock block in the same direction. A wave velocity meter, called HY-YS4A, was used to measure the longitudinal wave velocity of the specimens and remove the unqualified specimens. After the specimen selection, the prefabricated notch of 13.5 mm in length and 0.4 mm in width was introduced in the middle of the specimens by a thin diamond wire saw with a diameter of 0.3 mm (Fig. 2).

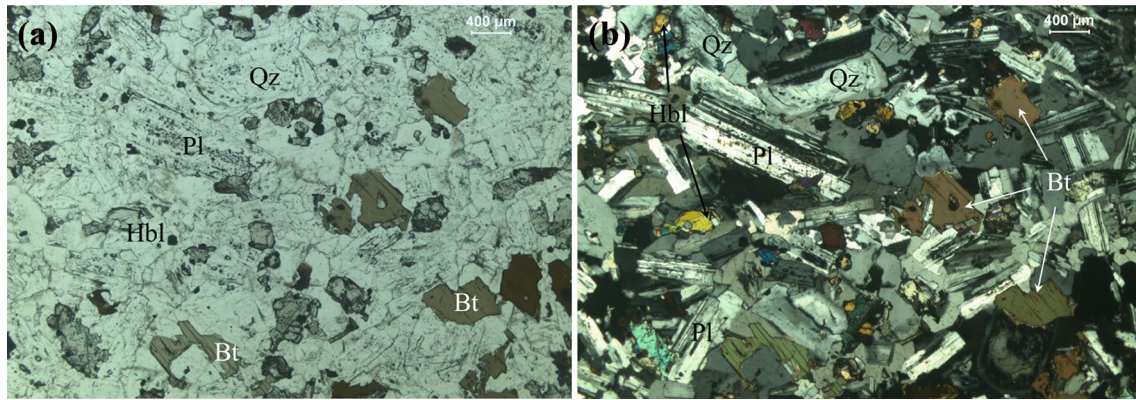


Fig. 1 Micrographs of the quartz-diorite under **a** plane-polarized light, and **b** cross-polarized light (After Wu et al. 2022c)

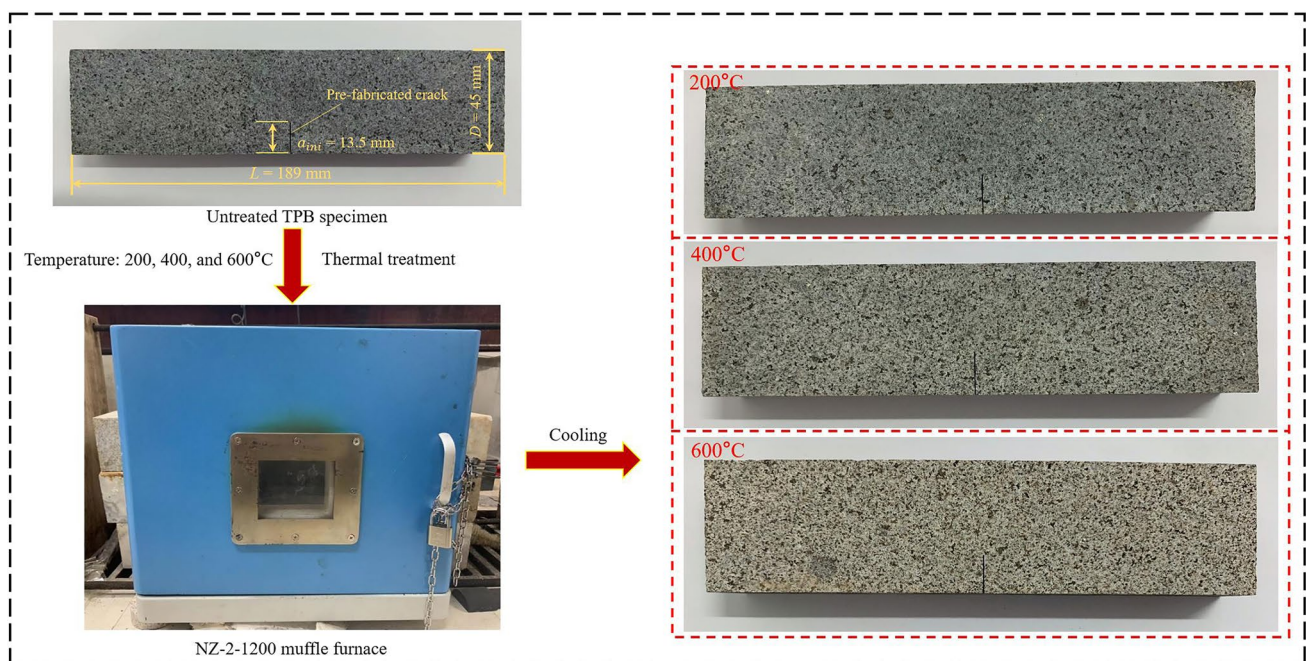


Fig. 2 Heating procedures and the TPB specimens under different temperatures

The specimens were then moved to thermal treatment with the help of an electron furnace (NZ-2-1200, Nazhi Electromechanical) with a maximum heating temperature of 1200 °C. The thermal experiments contain four temperature groups, i.e. Untreated (approximate 25 °C), 200, 400, and 600 °C. The heating rate is 2 °C/min. When the temperature arrives at the designated temperatures, the specimens dwelled at the temperature for 2 h for forming the same temperature field inside the rock matrix, and, thereafter, the specimens were naturally cooled to room temperature. The whole heating procedures and the specimens after different thermal treatments are shown in Fig. 2. It should be noted that the geometric parameters of

the specimens will change due to the heat dilatation, and thus the shape parameters of the specimens need to be re-measured before the mechanical test. Moreover, although the specimens endure a high temperature of 600 °C, in this work, no obvious macro-cracks develop on the specimen surfaces.

2.2 Experimental Setup and Loading Procedures

The overview of the testing setup is presented in Fig. 3. The experiments were carried out on the INSTRON-1342 servo control testing machine in the Advanced Research Center of Central South University. Each temperature group

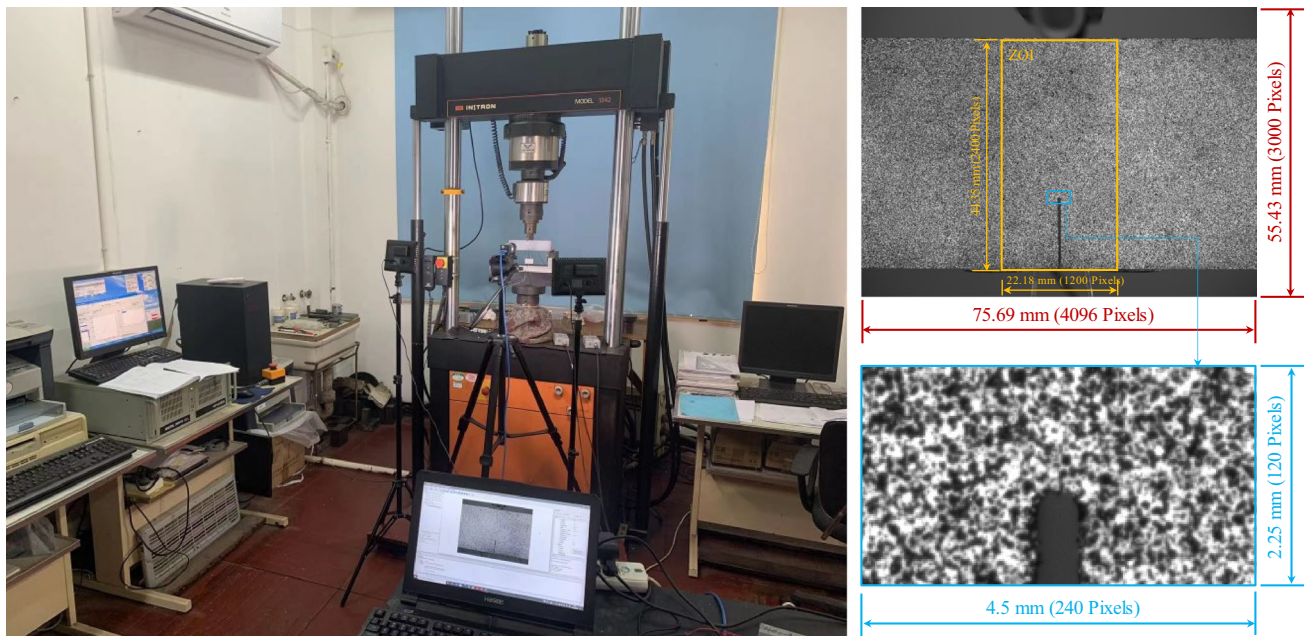


Fig. 3 Experimental setup and zone of interest (ZOI)

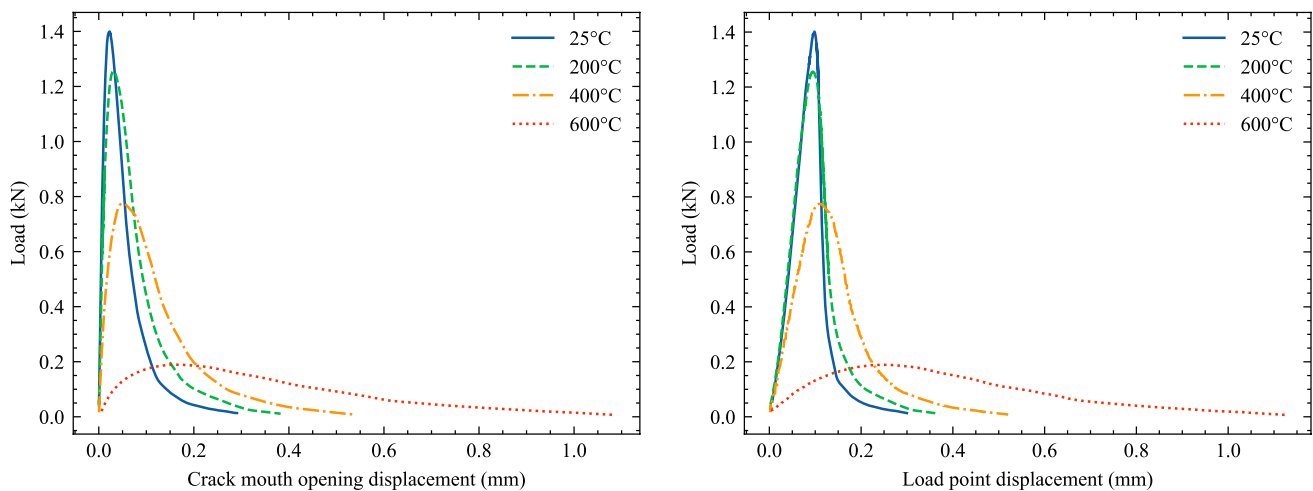
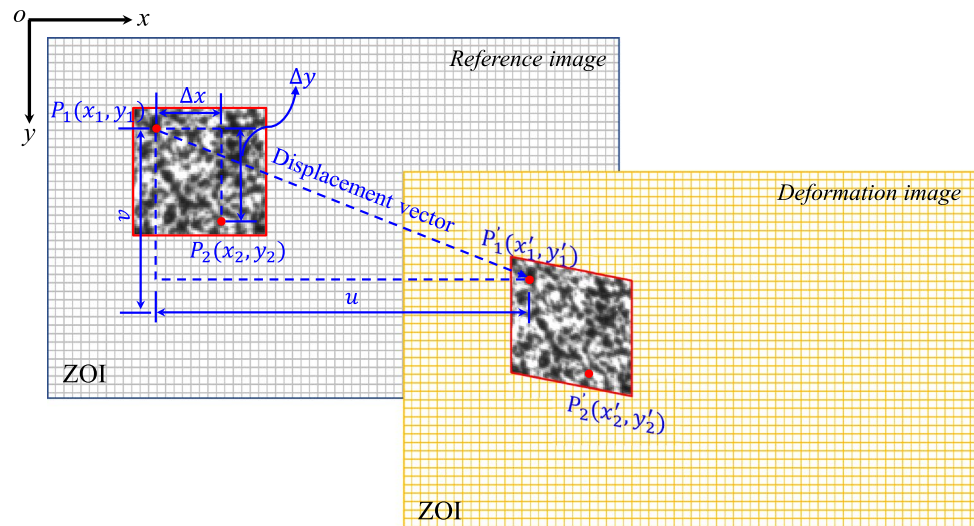
contains 3 three-point bend (TPB) specimens (a total of 12 specimens). A TPB test fixture with unfixed roller support was used for the fracture tests to avoid the potential friction effect (Bahrami et al. 2020). The span length was set as $4.0D$. A clip extensometer with a maximum range of 2.5 mm was mounted on the bottom of the specimen to collect the CMOD. The axial load P was recorded by the load cell installed on the framework of the testing machine. The loading rate of 0.05 mm/min at the top centre of the beam was applied to avoid the inertia effect and form a steady crack propagation. The fracture tests stop when the axial load is less than 10N.

The DIC technique has been widely applied in fracture tests because it has the characteristics of contactless, real-time and high precision (Wu et al. 2011; Yan et al. 2021; Zhu et al. 2022a; Feng et al. 2022; Chen et al. 2022). In this text, a 2D-DIC system composed of a global shutter complementary metal–oxide–semiconductor (CMOS) transistor camera (4096×3000 pixels, ME2P-1230-23U3M, Daheng Imaging Technology Co. LTD, China), an imaging lens (Computar V5024-MPZ, CBC Co. LTD, Japan) and two white fill lights, was applied to assess the crack propagation behaviours under the different loading phases with 5 frames per second and the exposure time of 40 ms. The random speckle pattern with white background and black speckle was printed on the surface and the typical image obtained by the DIC system was displayed in Fig. 3. The size of the zone of interest (ZOI)

is about $22.18 \times 44.35 \text{ mm}^2$ (1200×2400 pixels), and the most speckle size is in the range of 3–7 pixels. After the fracture experiments, the recorded images were processed with the help of an open-source 2D digital image correlation MATLAB program called Ncorr (Blaber et al. 2015) with a Subset radius of 45 and Subset spacing of 3. The DIC program can match the subsets between the reference image and the deformation image in the ZOI, as shown in Fig. 4. In Ncorr, the Normalized Cross Correlation (NCC) algorithm is used to correlate the subsets on the reference image and deformation image by the greyscale pattern intensity, and the Inverse Compositional Gauss–Newton (ICGN) method is adopted to refine the correlated results and calculate the strain based on displacement vectors. More information about the DIC program and the adopted algorithms can refer to the literature (Blaber et al. 2015).

2.3 Load–Displacement Curves and Fracture Characteristics Detected by the DIC Technique

The typical load-CMOD and load-LPD (load point displacement) curves of the TPB specimen after different temperatures are shown in Fig. 5, where the peak load of the specimens is among the middle in each temperature group. It can be seen that the peak load (P_{\max}) of the specimen decreases sharply with the increase of treatment temperatures, while the CMOD or LPD at peak load develops at an opposite trend.

Fig. 4 Schematic diagram of the DIC calculation**Fig. 5** Load-CMOD and Load-LPD (load point displacement) curves of TPB specimens under different temperatures, where the peak load of the specimens is among the middle in each temperature group

The horizontal strain fields of the TPB specimens under different loading phases detected by the DIC system are shown in Fig. 6. For specimens at 25 °C, the butterfly shape strain field occurs at the pre-peak stage of 50% peak load, which indicates that in this case, the specimen is almost in the linear elastic state. When the load reaches 100% peak load, we can observe that the crack has initiated from the pre-fabricated crack tip. With the increase in temperature, the nonlinear fracture behaviour becomes more and more significant and the 50% peak load is enough to motivate the crack extension for specimens at 400 °C and 600 °C. For specimens at 25 and 200 °C, the crack extension process is dominated by the single main crack. However, for specimens at 400 °C and 600 °C, the crack propagation path is more complex than those at 25 and 200 °C, and many branch

cracks can be observed during the loading process. Previous studies (Yin et al. 2019; Zhang et al. 2022b; Wu et al. 2020c; Shao et al. 2022; Zhuang et al. 2022; Yang et al. 2022) have examined the fracture morphology and fractal dimension of the specimen after different temperatures, and their results suggested that the fracture morphology become more and more complicated and the fractal dimension of fracture surface increases with the increase in temperature.

To further understand the fracture process of the specimens, the crack opening displacement profile under different loading phases was obtained based on the displacement gradient-based method (Wu et al. 2011). Figure 7 shows an example that determines the crack opening displacement (COD) profile of the TPB specimen at a temperature of 25 °C and the axial load of 100% peak load. As illustrated in

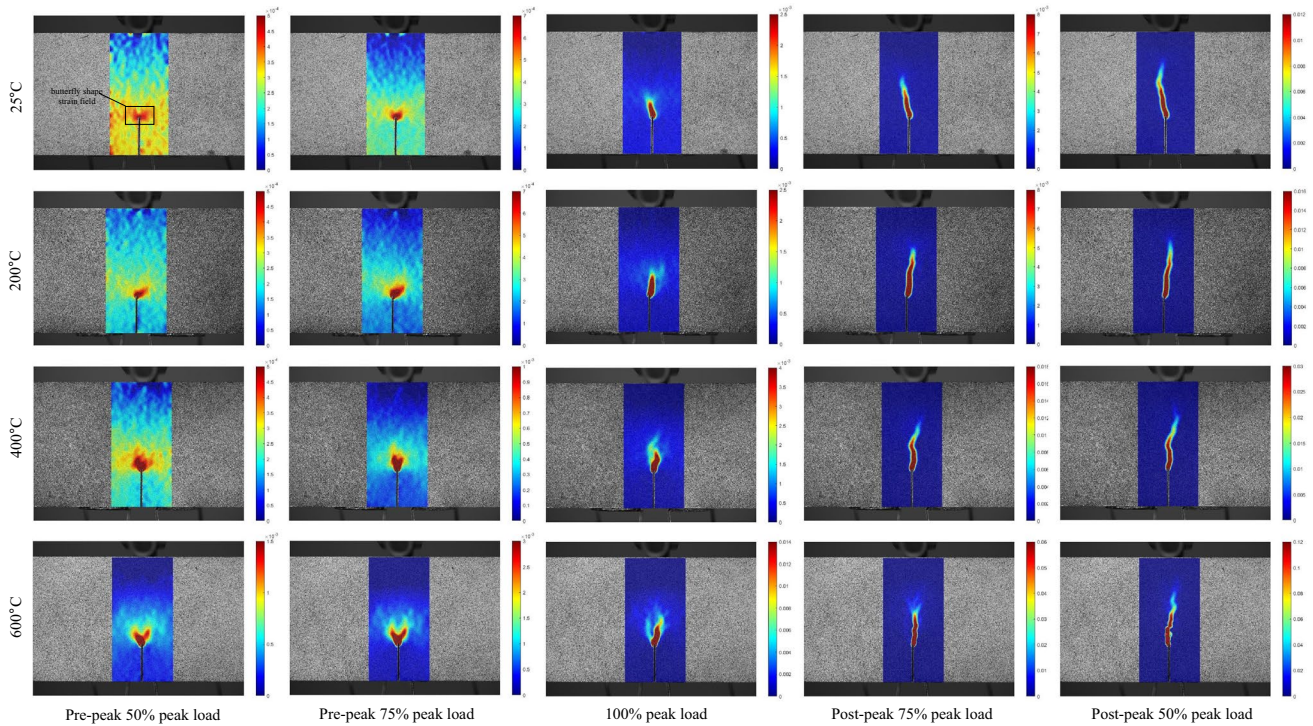


Fig. 6 Evolution of the horizontal strain field of TPB specimens under different temperatures

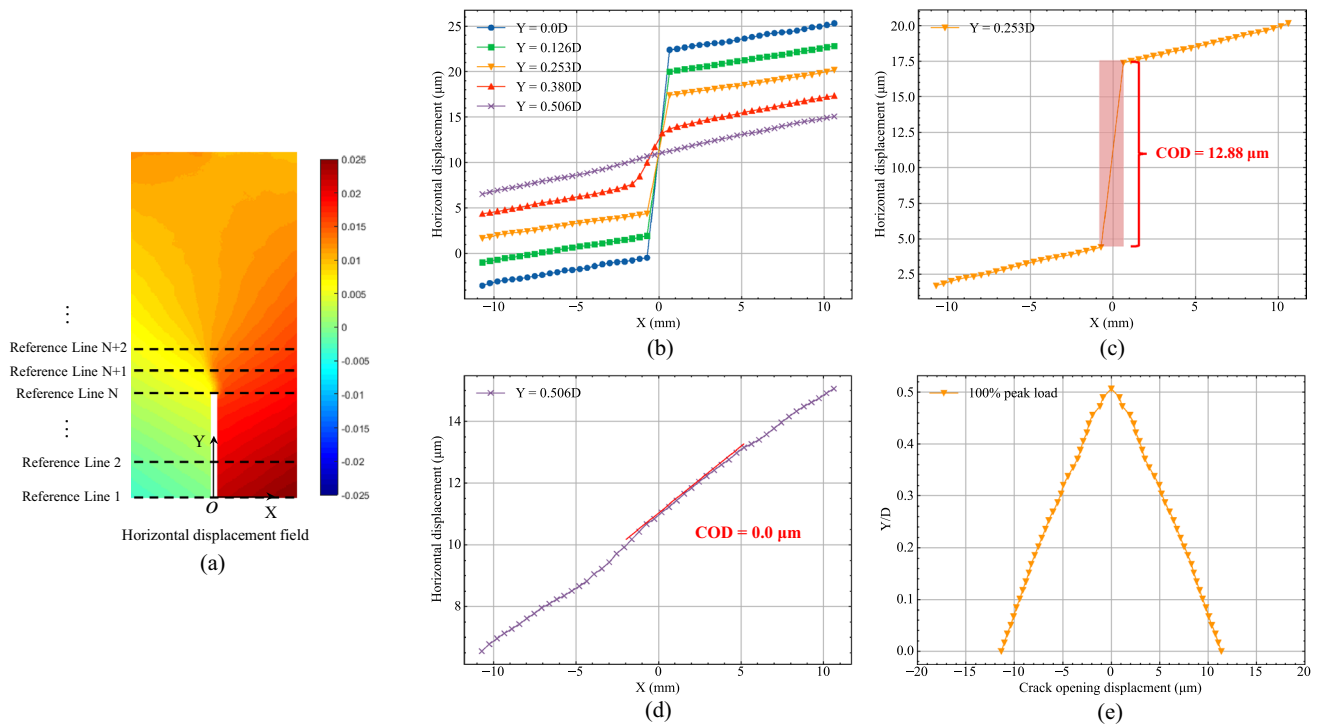


Fig. 7 Determination of crack opening displacement from the horizontal displacement field: **a** horizontal displacement contour image at a temperature of 25 °C and the axial load of 100% peak load; **b** hori-

zontal displacement at different reference lines; **c** horizontal displacement at $Y=0.253D$; **d** horizontal displacement at $Y=0.506D$; and **e** the obtained crack opening displacement profile at 100% peak load

Fig. 7a, many reference lines were arranged on the horizontal displacement field of the ZOI from the bottom to the top of the specimen. Figure 7b displays the horizontal displacement at $Y=0.0D, 0.126D, 0.253D, 0.380D,$ and $0.506D$. It is observed from Fig. 7b that there exists an obvious displacement jump for reference lines at $Y=0.0D, 0.126D, 0.253D,$ and $0.380D$, but the amplitude gradually decreases when moving the reference line from the bottom to the top of the ZOI. The COD can be inferred from the beginning and the ending of the displacement jump of the horizontal displacement (Wu et al. 2011). For example, in Fig. 7c, the displacement jump region is in the area of $0.714 \text{ mm} \leq X \leq 0.645 \text{ mm}$, and therefore, the COD is calculated to be $12.88 \text{ }\mu\text{m}$. Using the same method, the tip of the fracture process zone (FPZ) or the coordinate of the crack tip can be determined. As shown in Fig. 7d, at $Y=0.506D$,

the horizontal displacement changes smoothly, and no displacement jump can be observed. The COD is regarded as $0.0 \text{ }\mu\text{m}$ and the position $Y=0.506D$ refers to the crack tip. The finally obtained COD profile is illustrated in Fig. 7e, where the interval of the adjacent reference line is $0.169D$.

The COD profiles under different loading phases and temperatures are presented in Fig. 8. For the specimen at $25 \text{ }^\circ\text{C}$, it can be observed when the specimen is under the pre-peak 50% peak load, there is almost no apparent crack extension. A similar phenomenon can be observed for the $200 \text{ }^\circ\text{C}$ specimens that no apparent crack extension when the specimen is at a load of pre-peak 50% peak load. However, for the 400 and $600 \text{ }^\circ\text{C}$ specimens, when the specimens are at a load of pre-peak 50% peak load, the crack tip coordinates locate at $0.348D$ and $0.481D$, respectively. Considering that the pre-fabricated crack notch is approximately $0.3D$, the

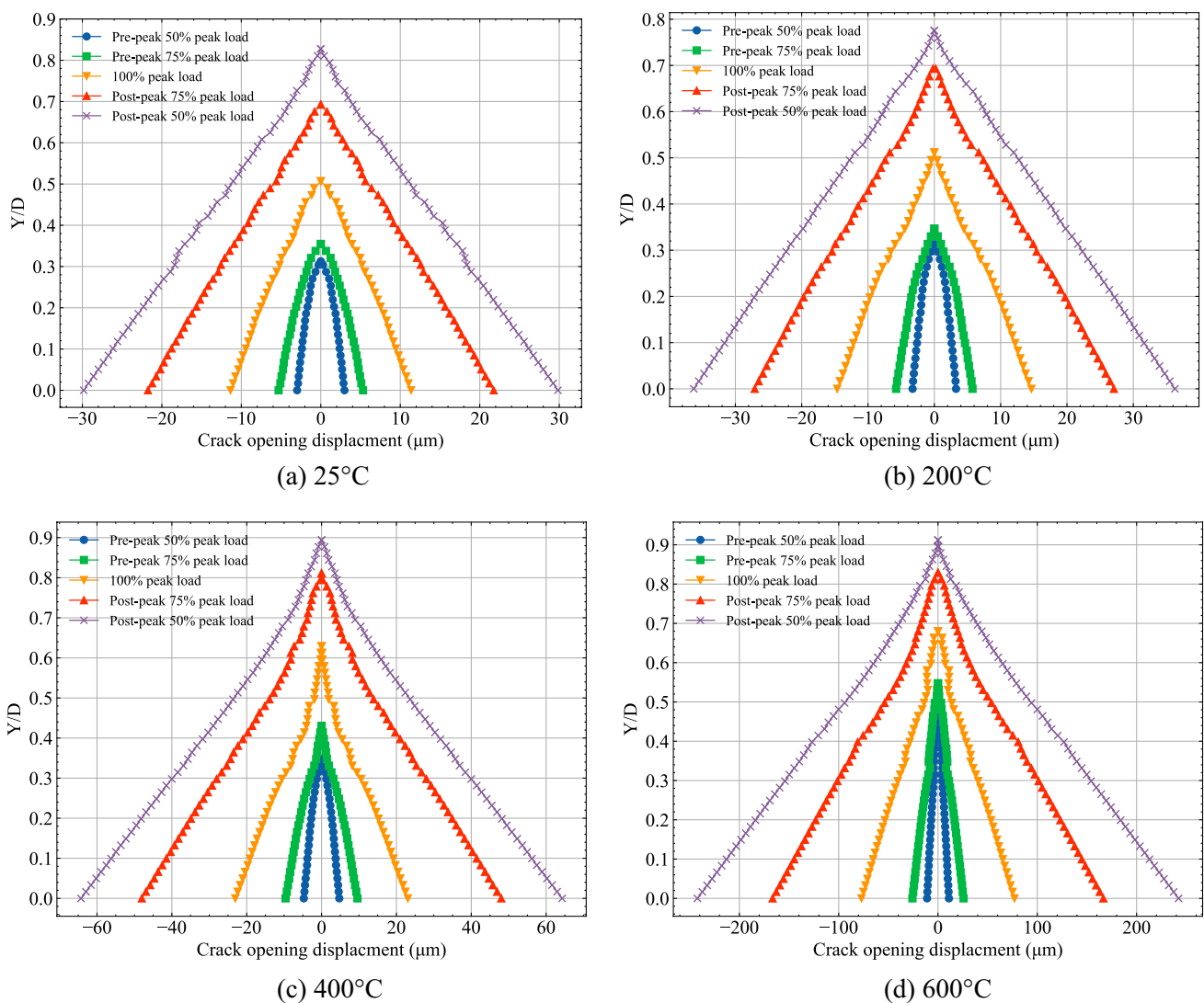


Fig. 8 Evolution of COD profiles of TPB specimens under different temperatures.

results indicate that the heat treatment decreases the crack initiation load for the specimens. Moreover, Fig. 8 shows that the crack length is positively correlated with the temperature for the specimens at the same exterior load level. For instance, when the specimens are at 100% peak load, the crack lengths are 0.506D, 0.512D, 0.629D, and 0.680D for the specimens at 25, 200, 400, and 600 °C, respectively. It should be noted that conventional linear elastic fracture mechanics (LEFM) are frequently used to describe the fracture failure of rock specimens at normal temperature conditions. Since the conventional LEFM uses the peak load and the initial crack length to compute the fracture toughness, the discrepancy between the true fracture resistance at peak

2018, 2021; Wu et al. 2014, Wang et al. 2019). Therefore, in the following, we employ this criterion to solve the tension softening curves and the crack propagation process of thermally treated specimens. For mode I crack, the initial fracture toughness criterion can be expressed as (Xu and Reinhardt 1999; Dong et al. 2013; Yin et al. 2023):

$$K_{IC}^{ini} = K_I^P - K_I^c \quad (1)$$

where K_I^P is the effective stress intensity factor caused by the remote load P , which can be estimated according to the effective crack model (ECM) (Karihaloo and Nallathambi 1990). For TPB specimen adopted in the present study, it can be calculated using the following formula (Tada et al. 2000):

$$K_I^P(a) = \frac{3PS\sqrt{\pi a}}{2D^2B} F\left(\frac{a}{D}\right), F\left(\frac{a}{D}\right) = \frac{1}{\sqrt{\pi}} \frac{1.99 - \left(\frac{a}{D}\right)\left(1 - \frac{a}{D}\right) \left[2.15 - \frac{3.93a}{D} + 2.7\left(\frac{a}{D}\right)^2\right]}{\left(1 + \frac{2a}{D}\right)\left(1 - \frac{a}{D}\right)^{\frac{3}{2}}} \quad (0 \leq \frac{a}{D} < 1), \quad (2)$$

load and that calculated based on the conventional LEFM theory will widen with the increase in temperature. Besides, the fracture toughness might be a function of the exterior load or the crack length (Wei et al. 2016; Zhao et al. 2022). Recently, Zhao et al. (2022) investigated the effect of notch geometry on the crack initiation and propagation characteristics of semi-circular bend specimens by mean of the DIC technique and calculated the crack resistance curve before the peak load, and their results indicated that the fracture toughness increases with the increase in the effective crack length or the FPZ length. Therefore, when a single fracture toughness value is used, it might not be enough to describe the complete fracture process of the specimen.

In the following sections, the fracture process of the specimens is tried to be further understood with the help of the initial fracture toughness criterion (Xu and Reinhardt 1999; Dong et al. 2013; Yin et al. 2023).

3 Inverse Analysis Approach and Determination of Tension Softening Curve

3.1 Brief Introduction to the Inverse Analysis Method

To obtain the tension softening function, an appropriate fracture criterion should be applied to describe the fracture processes of rock specimens. Many studies indicate that the initial fracture toughness criterion can effectively describe the fracture processes of rock-like material under pure mode I loading (Jeng and Shah 1985; Dong et al. 2013, 2016,

where a is the effective crack length, B is the specimen thickness, D is the specimen depth, and S is the span length.

K_{IC}^{ini} denotes the initial fracture toughness, which is given as follows:

$$K_{IC}^{ini} = \frac{3P_{ini}S\sqrt{\pi a_{ini}}}{2D^2B} F\left(\frac{a_{ini}}{D}\right), \quad (3)$$

where P_{ini} denotes the initial cracking load and a_{ini} is the initial crack length.

K_I^c is the cohesive stress intensity factor, which is generated by the cohesive stress in the FPZ, and it can be determined using Green's function (Jeng and Shah 1985) as follows:

$$\begin{aligned} K_I^c(a, a_e) &= 2 \int_{a_e}^a \frac{\sigma[w(u)]}{\sqrt{\pi a}} G\left(\frac{u}{a}, \frac{a}{D}\right) du, G\left(\frac{x}{a}, \frac{a}{D}\right) \\ &= \frac{3.52\left(1 - \frac{x}{a}\right)}{\left(1 - \frac{a}{D}\right)^{\frac{3}{2}}} - \frac{4.35 - 5.28\frac{x}{a}}{\left(1 - \frac{a}{D}\right)^{\frac{1}{2}}} \\ &\quad + \left\{ \frac{1.30 - 0.30\left(\frac{x}{a}\right)^{\frac{3}{2}}}{\sqrt{1 - \left(\frac{x}{a}\right)^2}} + 0.83 - 1.76\frac{x}{a} \right\} \\ &\quad \left[1 - \left(1 - \frac{x}{a}\right)\frac{a}{D} \right], \end{aligned} \quad (4)$$

where w is the crack opening displacement, $\sigma[w(x)]$ is the cohesive stress at point x , $a_e = a - L_{FPZ}$ and $G\left(\frac{x}{a}, \frac{a}{D}\right)$ is the Green's function. The Green's function for other geometries

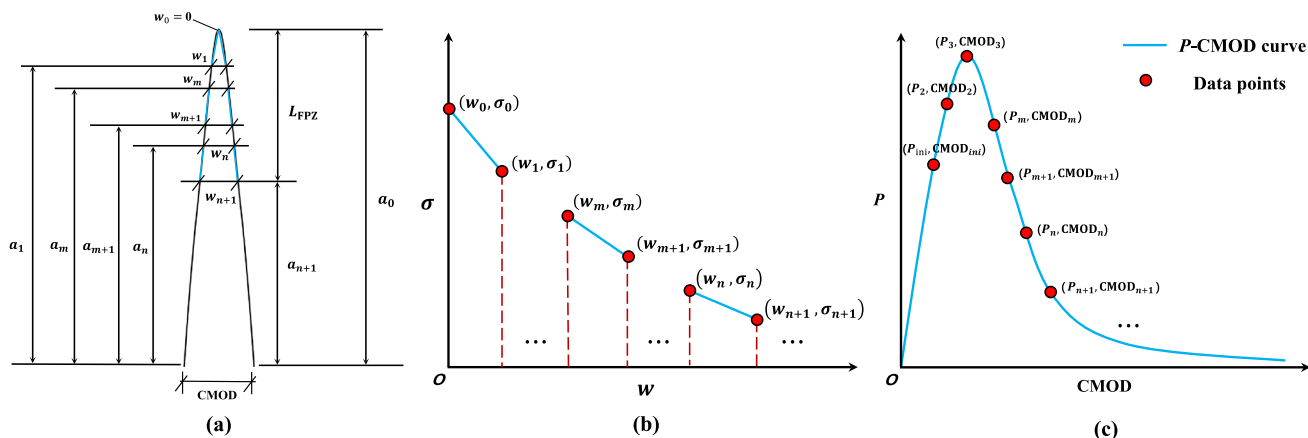


Fig. 9 **a** Schematic diagram of piecewise linear crack opening displacement, **b** Schematic diagram of piecewise linear $\sigma - w$ relation, and **c** Data points obtained from P -CMOD curve for determination of $\sigma - w$ relation

might be obtained based on the methods described by Shen and Glinka (1991), Jing and Wu (2015), and Wu et al (2018a).

The load P promotes the opening of the crack plane, and the cohesive stress exerts a negative effect. Considering the two effects, based on the linear superposition principle, the crack opening displacement $w(x)$ can be written as follows (Mai 2002; Wang et al. 2019):

In Eqs. (6) and (7), it can be found that the P -COMD relation is related to the tension constitutive law, i.e. $\sigma(w)$. However, the $\sigma - w$ relation cannot be directly calculated using the experimental P -CMOD results, because the calculation of crack opening displacement w involves solving the complex implicit equation (Eq. (5)). Wang et al. (2019) and Li et al. (2021) suggested that the $w(x)$ is a linear function, and the calculation procedures are simplified.

$$w(x) = \begin{cases} \frac{6PS}{ED^2B} \int_x^a F\left(\frac{u}{D}\right) G\left(\frac{x}{u}, \frac{u}{D}\right) du - \frac{8}{\pi E} \int_x^a \int_{a_e}^u \frac{\sigma[w(v)]}{u} G\left(\frac{v}{u}, \frac{u}{D}\right) G\left(\frac{x}{u}, \frac{u}{D}\right) dv du & \text{for } a_e \leq x < a \\ \frac{6PS}{ED^2B} \int_x^a F\left(\frac{u}{D}\right) G\left(\frac{x}{u}, \frac{u}{D}\right) du - \frac{8}{\pi E} \int_{a_e}^a \int_{a_e}^u \frac{\sigma[w(v)]}{u} G\left(\frac{v}{u}, \frac{u}{D}\right) G\left(\frac{x}{u}, \frac{u}{D}\right) dv du & \text{for } 0 \leq x < a_e \end{cases}, \tag{5}$$

where E is the elastic modulus.

Combining Eqs. (1)-(5), the load P and the crack mouth opening displacement (CMOD) result in the following:

$$P = \frac{2D^2B}{3S\sqrt{\pi a}F(a/D)} \left\{ K_{IC}^{ini} + 2 \int_{a_e}^a \frac{\sigma[w(u)]}{\sqrt{\pi a}} G\left(\frac{u}{a}, \frac{a}{D}\right) du \right\}, \text{ and} \tag{6}$$

However, It can be seen from Fig. 8 that the $w(x)$ does not vary linearly as expected. The linear assumption may yield an inaccurate result of $w(x)$ and generate an unreliable result of $\sigma(w)$. Therefore, to precisely determine the $\sigma - w$ relation, the piecewise linear crack profile (Zhang et al. 2010) (Fig. 9a) is applied as follows:

$$CMOD = \frac{6PS}{ED^2B} \int_0^a F\left(\frac{u}{D}\right) G\left(0, \frac{u}{D}\right) du - \frac{8}{\pi E} \int_{a_e}^a \int_{a_e}^u \frac{\sigma[w(v)]}{u} G\left(\frac{v}{u}, \frac{u}{D}\right) G\left(0, \frac{u}{D}\right) dv du. \tag{7}$$

$$w(x) = \frac{w_{i+1} - w_i}{a_{i+1} - a_i} (x - a_i) + w_i \text{ for } a_{i+1} \leq x \leq a_i \ (i = 0, 1, \dots, n), \tag{8}$$

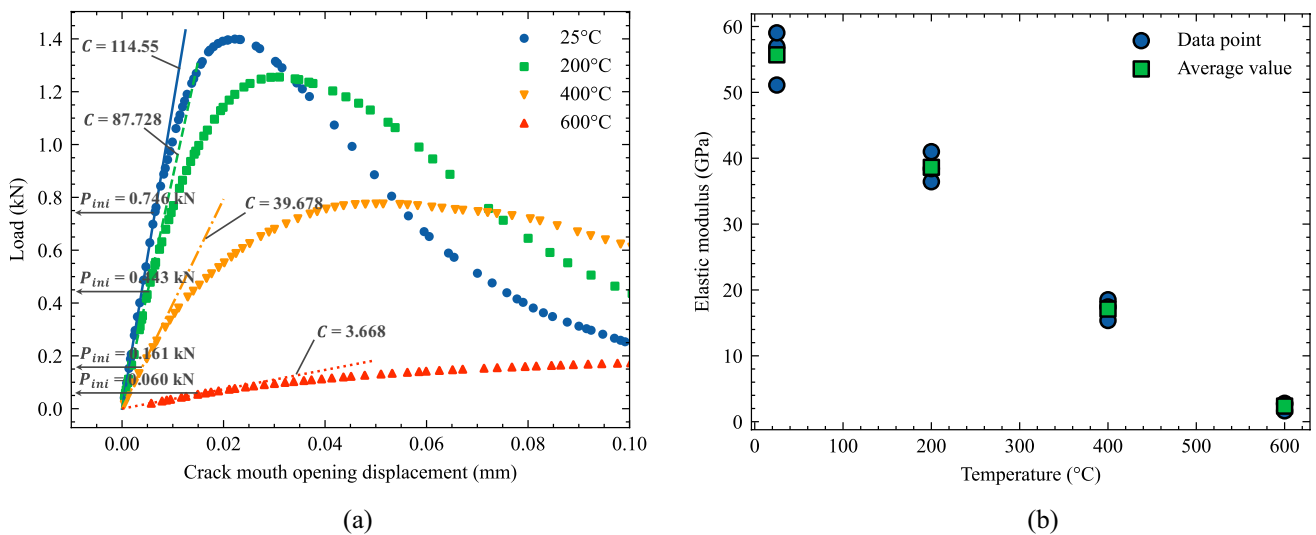


Fig. 10 **a** Acquisition of the slope C and the initial cracking load P_{ini} , and **b** the elastic modulus of the TPB specimens under different temperatures

Table 1 Average elastic modulus, initial fracture toughness, and tensile strength of quartz-diorite specimen under different temperatures

Temperature (°C)	25	200	400	600
Elastic modulus (GPa)	59.05	40.84	18.14	2.52
Initial fracture toughness (MPa·m ^{1/2})	0.955	0.404	0.182	0.044
Tensile strength (MPa)	9.83	8.71	5.39	1.10

where $a_0 = a$, $a_{n+1} = a_e$, and the crack opening displacement at the point a_i must satisfy the following:

$$w(a_i) = \frac{6PS}{ED^2B} \int_{a_i}^a F\left(\frac{u}{D}\right) G\left(\frac{a_i}{u}, \frac{u}{D}\right) du - \frac{8}{\pi E} \int_{a_i}^a \int_{a_e}^u \frac{\sigma[w(v)]}{u} G\left(\frac{v}{u}, \frac{u}{D}\right) G\left(\frac{a_i}{u}, \frac{u}{D}\right) dv du = w_i \quad (i = 1, \dots, n). \tag{9}$$

The $\sigma - w$ relation (Fig. 9b) might be also expressed by a similar piecewise linear function (Zhang et al. 2010; Chen and Su 2013) as follows:

$$\sigma(w) = \frac{\sigma_{i+1} - \sigma_i}{w_{i+1} - w_i} (w - w_i) + \sigma_i \quad \text{for } w_i \leq w \leq w_{i+1} \quad (i = 0, 1, \dots, n), \tag{10}$$

where σ_0 is equal to the rock's tensile strength σ_t and $w_0 = 0$.

Therefore, when the specimen shape, the mechanical properties, and the cohesive law are known, by alteration of the crack length a , the P -CMOD curve of the specimen can be derived from the above equations. Similarly, when the P -CMOD curve of a specimen is known, the $\sigma - w$ relation can be also determined. The detailed calculation procedures are shown as follows:

- (a) Determine elastic modulus E , initial fracture toughness K_{IC}^{ini} and tensile strength σ_t .
- (b) Extract $(P_i, CMOD_i)$ ($i = 1, 2, \dots, n$) data from the P -CMOD curve, as shown in Fig. 9c.
- (c) Assume the crack tip moves from a_{ini} to a_1 , and substitute $a = a_i$, $P = P_1$ and $CMOD = CMOD_1$ into Eqs. (5)-(7) to solve the parameters w_1 and σ_1 .
- (d) Assume the crack tip move from a_n to a_{n+1} , and substitute $a = a_{n+1}$, $P = P_{n+1}$ and $CMOD = CMOD_{n+1}$, into Eqs. (5)-(7) to solve the parameters w_{n+1} and σ_{n+1} , in which the new a_i ($i = 1, 2, \dots, n$) should be determined from Eq. (9).

- (e) Repeat Step (d) until $\sigma_{n+2} \leq 0$.

It should be noted that in the above calculation pro-

cedures, the end of the FPZ will be constant, i.e. $a_e \equiv a_{n+1} \equiv a_{ini}$.

3.2 Elastic Modulus

Figure 10a shows the initial loading segments of the P -CMOD curves for the TPB specimens after different thermal treatments. It can be seen from Fig. 10a that load

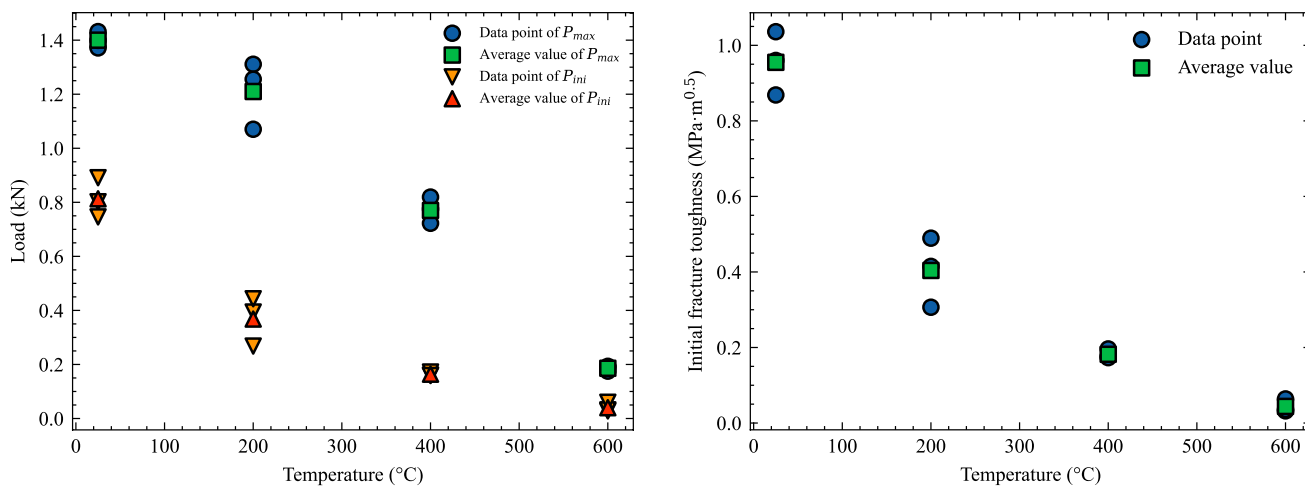


Fig. 11 a P_{ini} and P_{max} , and b K_{IC}^{ini} results

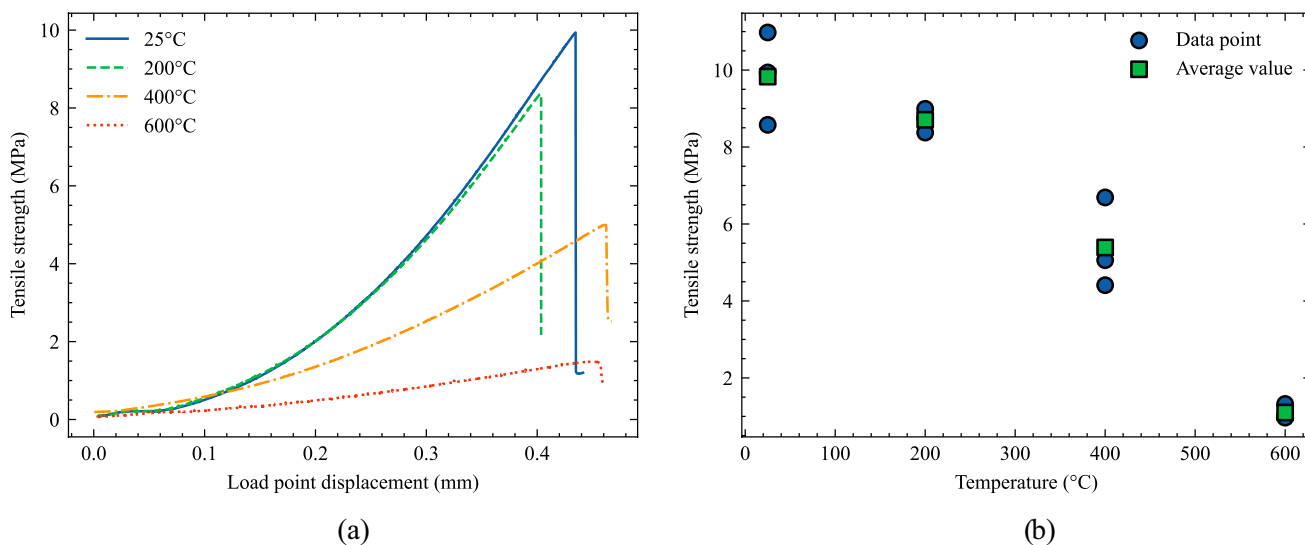


Fig. 12 a Typical tensile strength-displacement curves, and b tensile strength of the rock under different temperatures

P develops linearly with the alteration of the CMOD at the initial loading stage. Based on the horizontal strain field and the COD profile shown in Figs. 6, 8, it can be inferred that the crack has not initiated from the pre-fabricated crack tip at the initial loading stage. Therefore, at the early loading stage, it is assumed the crack propagation length can be neglected, i.e. $L_{FPZ} = 0$, $a = a_{ini}$, and $a_e = a_{ini}$. In Eq. (7), let $a = a_{ini}$ and $a_e = a_{ini}$, the CMOD can be expressed as the function of load P :

$$CMOD = \frac{6PS}{ED^2B} \int_0^{a_{ini}} F\left(\frac{u}{D}\right)G\left(0, \frac{u}{D}\right)du. \quad (11)$$

Since the elastic modulus E of the TPB specimen is constant, the formula indicates that if the crack has not initiated

from the prefabricated crack tip, the CMOD will develop linearly with the increase of P . If the crack has initiated from the crack tip, there would be a nonlinear relation between CMOD and P . Equation (11) was used to estimate the elastic modulus E of the TPB specimens. By rearranging Eq. (11), the following equation holds:

$$E = C \frac{6S}{D^2B} \int_0^{a_{mi}} F\left(\frac{u}{D}\right)G\left(0, \frac{u}{D}\right)du, C = \frac{P}{CMOD}. \quad (12)$$

In this paper, a linear function was used to fit the initial loading stage ($P \leq 25\%P_{max}$) of the P -CMOD curves and the slope (C) of the linear function was substituted into Eq. (12) with the geometry and loading parameters to compute the elastic modulus of a specimen. The obtained

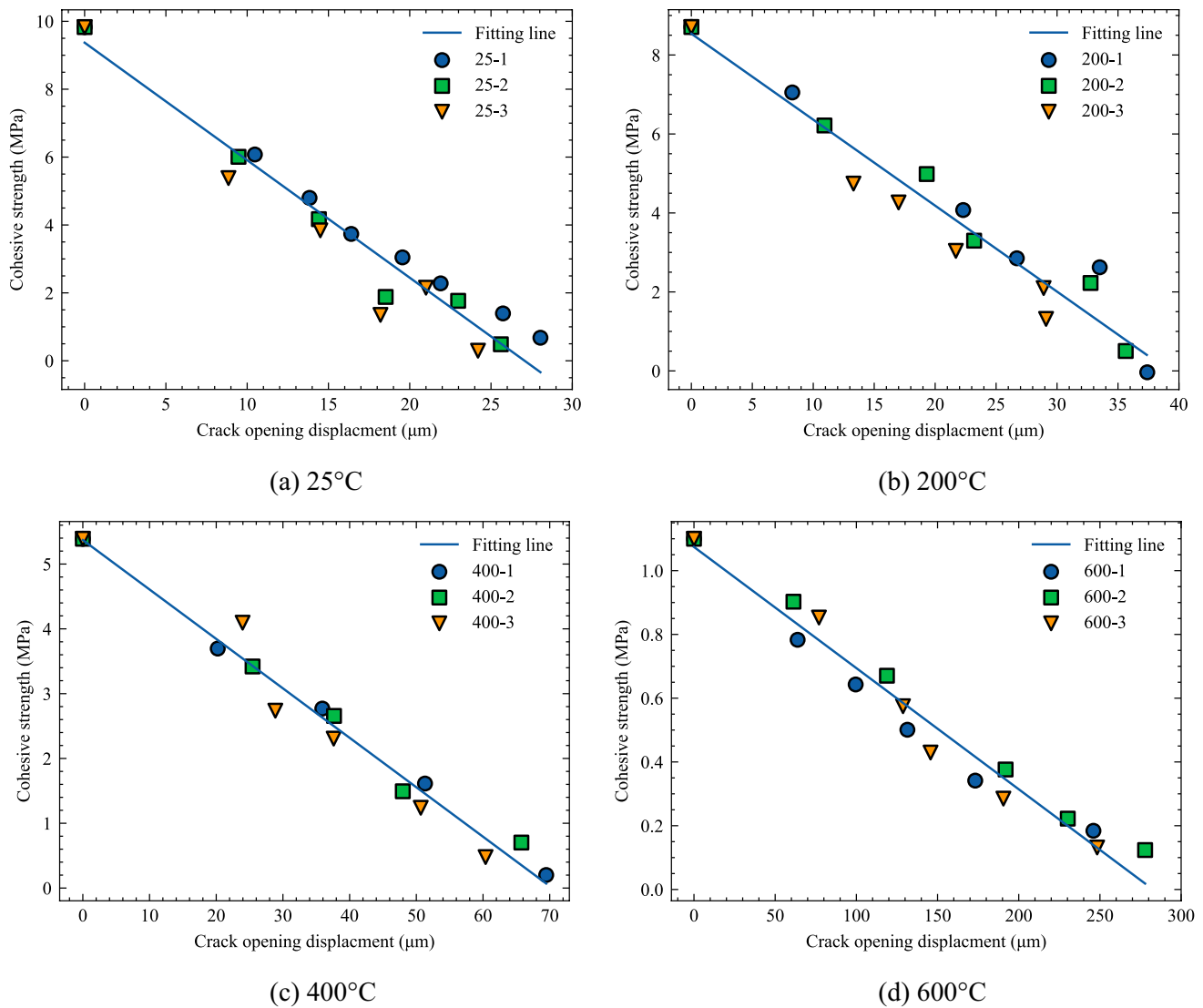


Fig. 13 Tension softening functions for quartz-diorite specimens under different temperatures.

elastic modulus of the TPB specimens after different heat treatments is shown in Fig. 10b, and the average results are listed in Table 1.

3.3 Initial Fracture Toughness

The determination of the initial crack load P_{ini} is the prerequisite for the calculation of initial fracture toughness K_{IC}^{ini} (Eq. (3)). P_{ini} can be directly inferred from the P -CMOD curves. In Sect. 3.2, it can be found that the initial linear stage of the P -CMOD curves refers to the elastic stage where no crack extension occurs. With the further ascending of CMOD, P increases nonlinearly. As a consequence, the starting point of the nonlinear segment is regarded as the crack initiation

point (Xu and Reinhardt 1999), i.e. P_{ini} , see Fig. 10a. The data of P_{ini} and P_{max} are illustrated in Fig. 11a, and the calculated K_{IC}^{ini} results are presented in Fig. 11b, and the average data are listed in Table 1.

3.4 Tensile strength

The tensile strength of the specimens after different heat treatments was measured with the aid of the Brazilian disk (BD) specimens. There are 12 BD specimens with a diameter of 50 mm and thickness of 25 mm drilled from the same rock block for tensile strength testing. The BD specimens were equally divided into 4 groups to experience different thermal treatments same as the TPB specimens. After the thermal treatment, the BD specimens were loaded with the servo-control

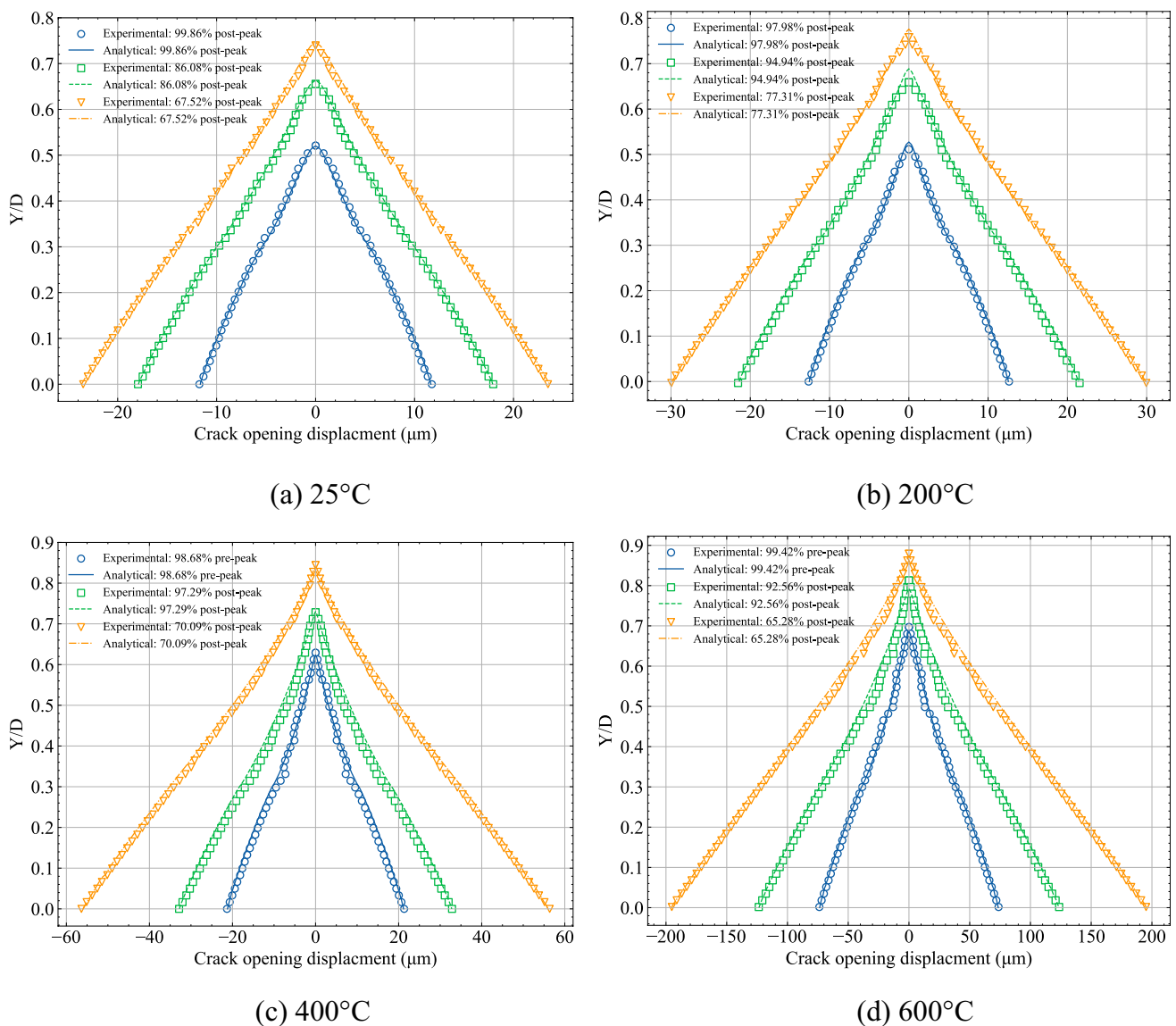


Fig. 14 Comparison of the experimental and analytical COD profiles under different loading phases.

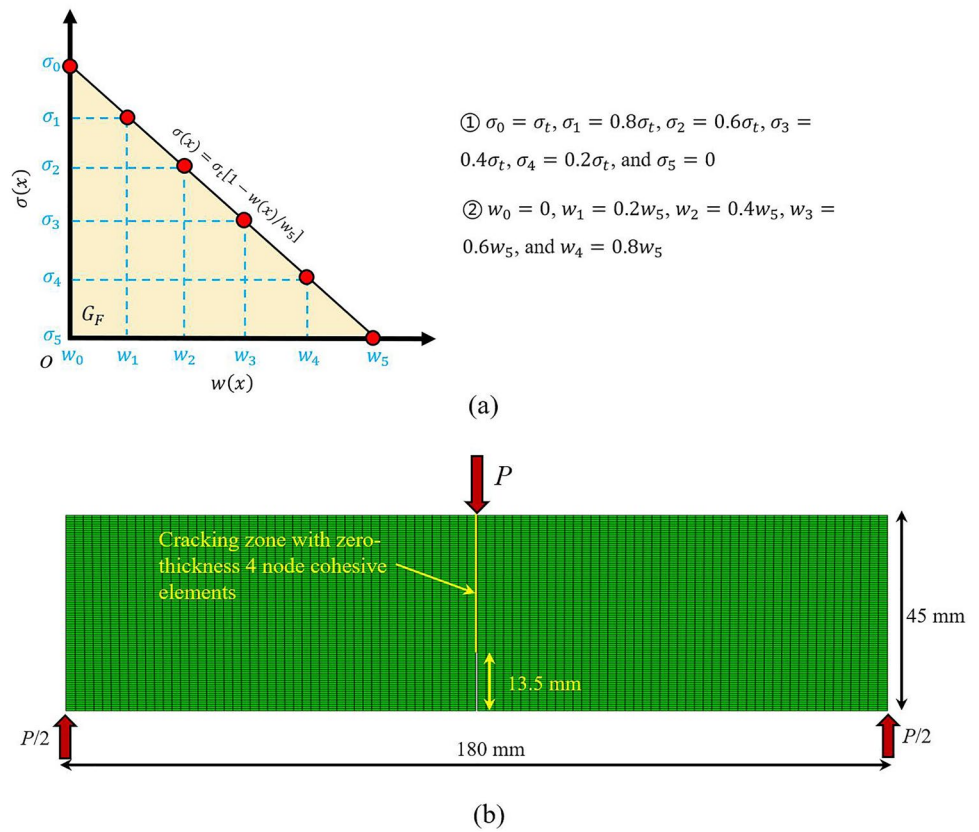
testing machine with an axial loading rate of 0.1 mm/min. The typical tensile strength-axial displacement curves are illustrated in Fig. 12a, the obtained tensile strength results were shown in Fig. 12b, and the average results are listed in Table 1. In the following analysis, the mean value of the tensile strength will be used for the calculation of the tension softening curves.

4 Tension Softening Curve and Verification

In this study, 4–7 data points were collected from the P -CMOD curves to calculate the tension softening curve. The obtained results are displayed in Fig. 13. It can be seen that the number of the used data points does not

affect the final results. To verify the effectiveness of the tension softening functions under different temperatures, the calculated crack opening displacement profiles were compared with that monitored by the DIC technique. It should be noted that although the piecewise linear crack profile was used in Eq. (8), the complete shape of the $w(x)$ can be still calculated from Eq. (5) when the boundary conditions, i.e. the distribution of the cohesive stress in the FPZ and the axial load, are given. In this regard, in each temperature condition, the COD results under three axial load conditions are calculated. The comparison of the experimental and analytical COD profiles is demonstrated in Fig. 14. From Fig. 14, it can be seen that analytical results coincide very well with the experimental,

Fig. 15 a The division of the tension-softening curve, and **b** the established finite element model in ABAQUS



which demonstrates that the distribution of the cohesive stress in the FPZ assumed in the study and the obtained results are reliable.

The tension softening curves of the TPB specimens under different high temperatures can be fitted with the linear function, and the linear fitting equation results under each temperature are shown as follows:

$$\left. \begin{aligned} \sigma(w) &= -0.3462w + 9.3715, R^2 = 0.9501 \quad (25^\circ\text{C}) \\ \sigma(w) &= -0.2177w + 8.5389, R^2 = 0.9519 \quad (200^\circ\text{C}) \\ \sigma(w) &= -0.0763w + 5.3704, R^2 = 0.9789 \quad (400^\circ\text{C}) \\ \sigma(w) &= -0.0038w + 1.0743, R^2 = 0.9712 \quad (600^\circ\text{C}) \end{aligned} \right\} \quad (13)$$

From Eq. 13, it can be observed that the goodness of fit reaches at least 0.95, which indicates that the cohesive strength follows a linear degradation mode with the increase in crack opening displacement. Comparing the tension softening curves of TPB specimens at different temperatures, it can be concluded that the tension softening curves are sensitive to thermal treatment. With the increase of the temperature, the intercept, i.e. the tensile strength, and the slope of the tension-softening curves decrease accordingly. The decrement in the tensile strength of rock specimens after different temperatures has been well-studied by researchers (Yin et al. 2015, 2022; Sirdesai et al. 2017; Mardoukhi

et al. 2017; Xu et al. 2020). Sirdesai et al. (2017) analyzed the variation of the tensile strength for different rocks after different temperatures, and they suggested that the decrease in the tensile strength for igneous rocks is mainly attributed to the expansion of the mineral grains. The expansion of the mineral grains might be also the reason for the decrease in the slope of the tension-softening curve with the increase in temperature. The slope of the tension-softening curve can be regarded as the stiffness of the specimen to withstand the crack from separation. The expansion of mineral grains can lead to debonding in mineral grains, which decreases the bond areas between the grains and thus, affects the stiffness of the specimen from the macroscopic perspective.

To further manifest the effectiveness of the obtained tension-softening curves. The obtained tension-softening curves are used to calculate the P -CMOD curves of the TPB specimens under different temperatures by two approaches. In the first method, the P -CMOD curves are calculated based on the analytical method presented in Sect. 3.1. It is known that the 4–5 data points collected from the experimental P -CMOD curves are enough to obtain the tension softening curve of the specimen. Therefore, the fitted tension softening curves were equally divided into five portions by the standard of the cohesive stress, as shown in Fig. 15a. In each

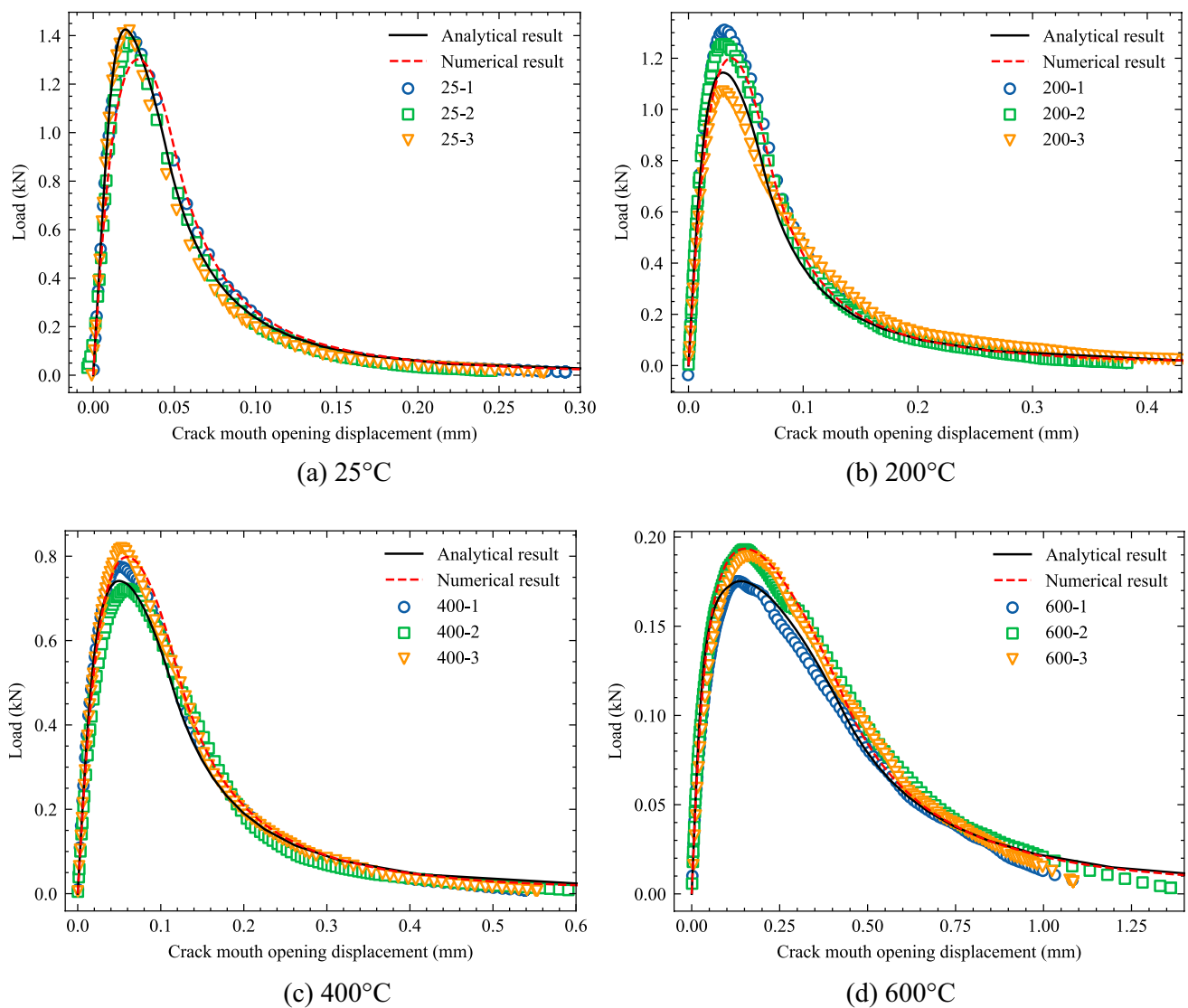


Fig. 16 Comparison of the analytical, numerical, and experimental P -CMOD curves under different temperatures.

portion, it is assumed that the variation of the cohesive stress and the crack opening displacement is linear. Combining the average elastic modulus E and initial fracture toughness K_{IC}^{ini} , by alteration of the crack length a , the P -CMOD curves can be acquired. In the second method, since the cohesive stress linearly declines with the increase of crack opening displacement, linear softening is applied in the numerical model. The stiffness of the cohesive element is set as 40×10^6 MPa/m to embody the rigid softening, and the onset of fracture is considered to be triggered only by tensile stress. Figure 15b shows the numerical model established in commercial finite element code ABAQUS, where the zero-thickness four-node cohesive elements are inserted into the predetermined crack-ing zone.

Figure 16 shows the comparison of the analytical, numerical, and experimental P -CMOD curves at different temperatures. It can be observed that the analytical and numerical P -CMOD curves coincide well with the experimental. There are some differences between the analytical and numerical P -CMOD curves. This is because the analytical approach is based on the boundary element method which is highly sensitive to Green's function, and, therefore, there exist some discrepancies between Green's function shown in Eq. (4) and the true results. However, it can be observed from Fig. 15 that the differences between the analytical and numerical P -CMOD curves are acceptable, and it is believed that the tension-softening curves and the fracture model can characterize the fracture behaviours of the TPB specimens under different temperatures.

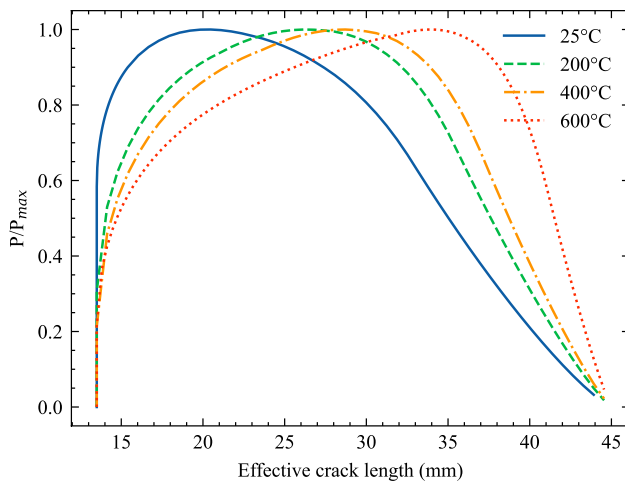
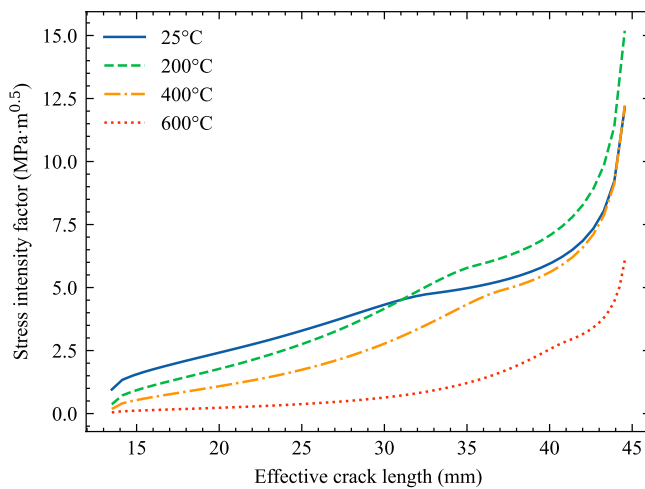


Fig. 17 The normalized load versus effective crack length curve under different temperatures

5 Analytical Assessment of Fracture Behaviours of TPB Specimens After Different High Temperatures

Since the fracture behaviour of TPB specimens can be well understood by the proposed tension softening curves, the tension softening curves is then used to further analyze the fracture process and the size effect on the fracture parameters of the TPB specimen under different temperatures.



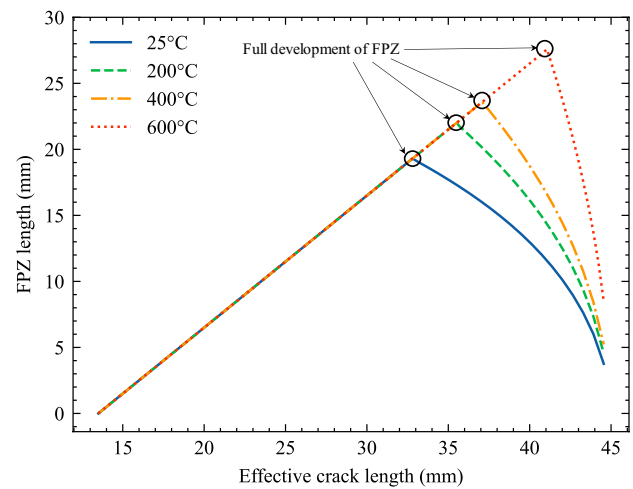
(a)

5.1 Effect of High Temperature on the Fracture Process of the TPB Specimens

The normalized load versus effective crack length curve is used to manifest the effect of thermal treatment on the fracture process of the TPB specimen with a depth of 45 mm. As shown in Fig. 17, the normalized load first increases and then decreases with the development of the effective crack length, and the start and end points of the curves at different temperatures are the same. With the increase in temperature, it is observed from the figure that the curve moves from left to right, and at the same loading condition, the higher temperature is, and the effective crack length at the same load level is higher, under the premise that the crack has initiated from the initial crack tip. For example, the crack lengths at peak load are 20.47, 26.17, 28.71, and 33.89 mm for specimens at 25, 200, 400, and 600 °C, respectively. The variation tendency of the crack length at peak load is consistent with the DIC results in Sect. 2.3.

5.2 Effect of High Temperature on the Development of the Effective Stress Intensity Factor and FPZ Length

The development of the stress intensity factor and the FPZ length with the effective crack length for the TPB specimens under different temperatures are shown in Fig. 18. As might be expected, the fracture resistance and FPZ length of the specimens are the functions of the effective crack length. It can be seen from Fig. 18a that the stress intensity factor first increases slowly and then increases



(b)

Fig. 18 a Stress intensity factor, and b FPZ length with effective crack length under different temperatures

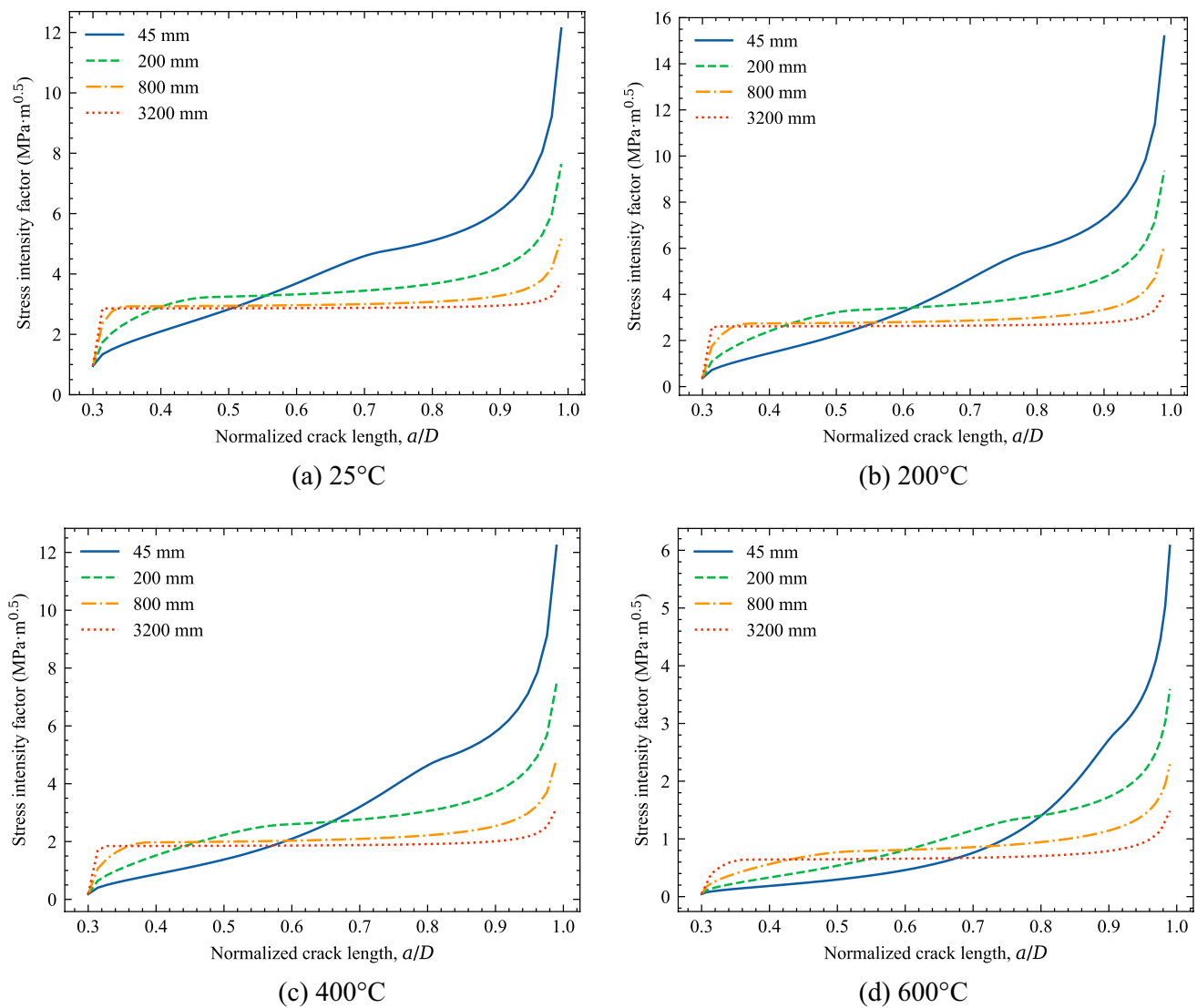


Fig. 19 Stress intensity factor with normalized crack length under different specimen depths.

rapidly with the increase of the effective crack length. When the crack length is less than about 31.05 mm, the stress intensity factor for the specimen at 25 °C is higher than that at 200 °C under the same crack length, while, when the effective crack length is higher than 31.05 mm, the stress intensity factor for the specimen at 200 °C is higher than that at 25 °C under the same crack length. With the increase in temperature, it is shown that $K_{I,25^{\circ}\text{C}}^P$ or $K_{I,200^{\circ}\text{C}}^P > K_{I,400^{\circ}\text{C}}^P > K_{I,600^{\circ}\text{C}}^P$. The FPZ length first increases and then decreases with the change in the crack length (Fig. 18b). The change point in the development of FPZ length corresponds to the point of the full development of FPZ where the traction-free crack will form at the pre-fabricated crack tip. The effective crack lengths at the moment of the full development of FPZ are 32.80, 35.50, 37.09, and 41.07 mm for 25, 200, 400, and 600 °C,

respectively, which is higher than that at peak load. This result indicates that the fully developed FPZ occurs at the post-peak stage of the TPB specimen.

5.3 Size Effect on the Fracture Toughness and FPZ Length for the Rock Specimens Under Different High Temperatures

In engineering practice, the mode I fracture toughness is one of the most important parameters to describe the fracture resistance of rock engineering structures at critical status (Zhang and Ouchterlony 2022). However, it was shown that for rock specimens under the laboratory scale, this value is specimen size and geometry-dependent (Ghoulfi et al. 2021; Wei et al. 2021, 2022). Therefore, the fracture resistance obtained by the 45 mm depth's TPB specimen might not

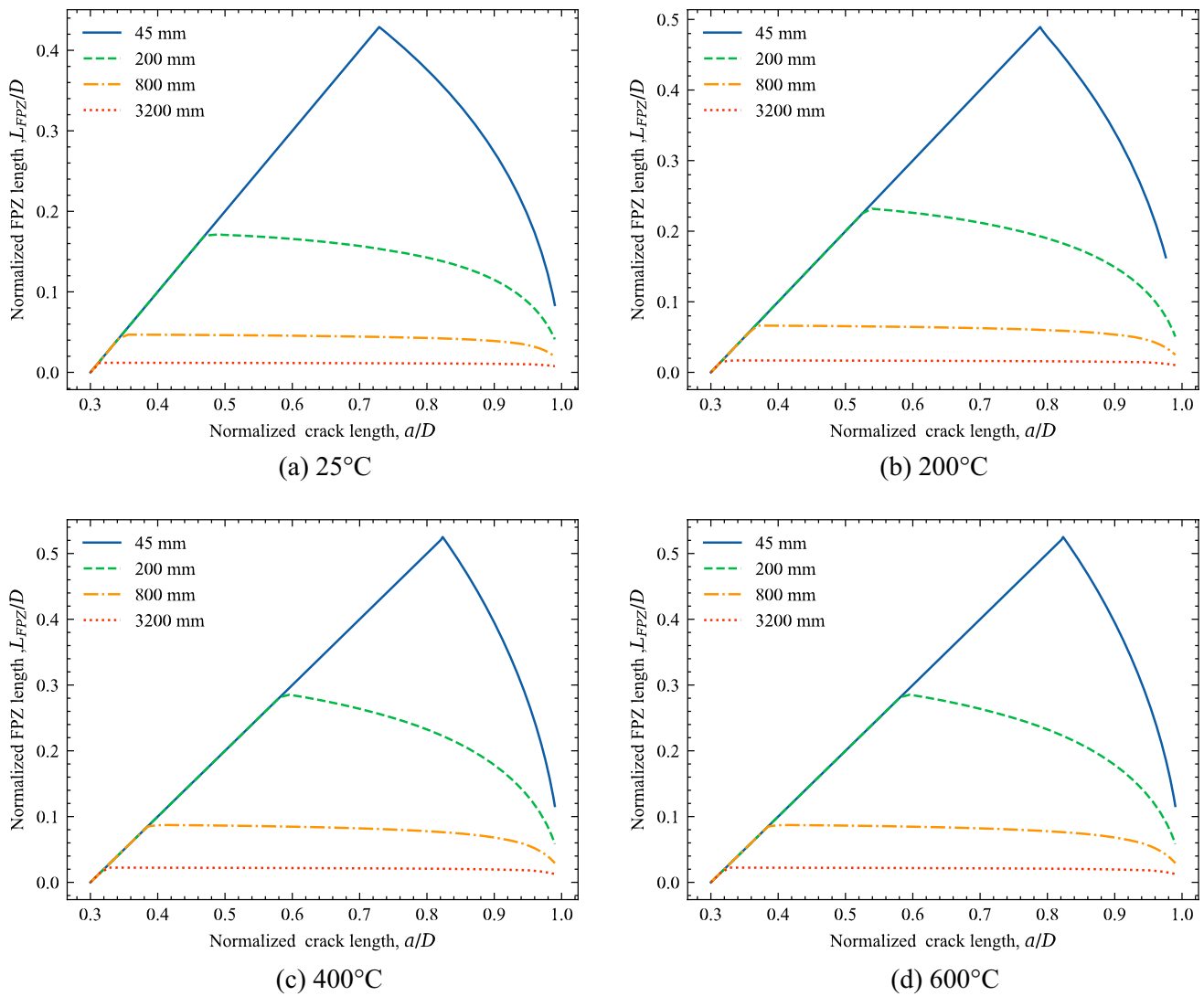


Fig. 20 Normalized FPZ length with normalized crack length under different specimen depths.

be able to describe the cracking behaviour for engineering scale rock engineering structures. When the tension-softening curve is known, it might be used to predict the fracture characteristics of TPB specimens under different specimen sizes. The obtained tension-softening curves are applied to compute the stress intensity factor and FPZ length vs. crack length curves of the geometry similar TPB specimens with $D=100, 200, 400, 800, 1600, 3200$, and 6400 mm, $a_{ini} = 0.3D$, and $S = 4.0D$.

As shown in Fig. 19, with the increase in the specimen depth, distinct platforms form in the stress intensity factor versus the normalized crack length curves. For specimens with a depth of 3200 mm, when $0.4 \leq a/D \leq 0.9$, the stress intensity factor is almost independent of the variation of the normalized crack length a/D . A similar phenomenon can be observed for the variation of the FPZ length for TPB specimens under different temperatures (Fig. 20).

For specimens under the depth of 45 and 200 mm, the normalized FPZ length decreases once the full FPZ has developed. However, for the specimen with a depth of 3200 mm, there exists a distinct platform in the a/D range of 0.4 to 0.9. Combining the development of the effective stress intensity factor and the FPZ length, it is possible to describe the entire fracture process for large-scale rock engineering structures by a single fracture toughness, which is size and crack length independent.

To further understand the size effect on the fracture toughness and the FPZ length, the fracture toughness and FPZ length at the peak load versus the specimen depth are demonstrated in Fig. 21. With the increase of specimen depth, the fracture toughness at peak load for specimen at 25 °C shows an increasing trend, while the fracture toughness at peak load for those at 200, 400, and 600 °C displays the decreasing trend (Fig. 21a). When the specimen

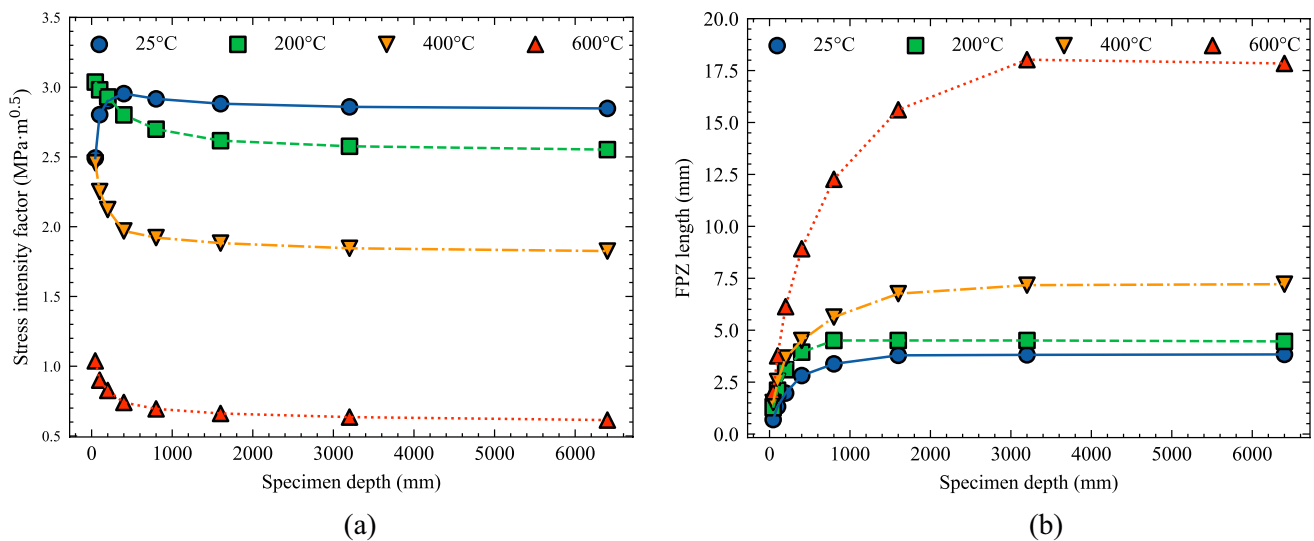


Fig. 21 **a** Fracture toughness, and **b** FPZ length at peak load with specimen depth under different temperatures

size is larger than 800 mm, the fracture toughness varies little, and $K_{I,25^{\circ}\text{C}}^{P_{\max}} > K_{I,200^{\circ}\text{C}}^{P_{\max}} > K_{I,400^{\circ}\text{C}}^{P_{\max}} > K_{I,600^{\circ}\text{C}}^{P_{\max}}$. Different from the fracture toughness results, all of the FPZ lengths are positively associated with the specimen depth. When the specimen depth is larger than or equal to 3200 mm, the FPZ length is almost independent of specimen depth. Moreover, Fig. 21b indicates that at any specimen depth, $L_{FPZ,25^{\circ}\text{C}}^{P_{\max}} < L_{FPZ,200^{\circ}\text{C}}^{P_{\max}} < L_{FPZ,400^{\circ}\text{C}}^{P_{\max}} < L_{FPZ,600^{\circ}\text{C}}^{P_{\max}}$. These results show that the size effect is a critical factor that should be taken into consideration in rock engineering where temperature matters.

6 Conclusions

Understanding the fracture and failure characteristics of rock engineering structures is of critical importance to the design, construction, and maintenance of rock engineering. In this work, an inverse method was adopted to solve the tension softening relation of the heat-treated quartz-diorite specimen using the P -CMOD curves from the TPB tests in which the inverse approach is established based on the pure analytical method and does not need to conduct finite element model analysis. The DIC technique was used to obtain the crack propagation parameters of the rock specimens and to verify the analytical results obtained from the inverse method under different loading stages. And further analyses on the fracture processes of heat-treated rock specimens have been accomplished based on the determined tension softening curves. The conclusions of the study are drawn as follows:

The shape of the tension-softening curve of the quartz-diorite specimen is not sensitive to thermal treatment. The cohesive stress changes linearly with the variation of the crack opening displacement. The heat treatment can only cause a decrease in the intercept, i.e. the rock tensile strength, and the slope of the tension-softening curves.

Combining experimental and analytical results, it was observed that the higher the temperature is, the crack is easier to develop at the pre-peak stage and the crack propagation length is higher at the same loading stages under the premise that the crack has initiated from the pre-fabricated crack tip.

The fracture toughness and FPZ length for the quartz-diorite specimens are the functions of the crack length. The fracture toughness monotonically increases with effective crack length, while the FPZ length first linearly increases before the form of complete FPZ and then decreases with the further increase in effective crack length, and the higher the temperature is, the larger the effective crack length is at the moment of full development of FPZ.

The fracture toughness and FPZ length at peak load are size dependent. For specimens at 25 °C, the fracture toughness at peak load increases with the specimen depth, while for those at 200, 400, and 600 °C, there is a negative relation between the fracture toughness and the specimen depth. Regarding the FPZ length, it was observed that the increase in specimen depth promotes the FPZ length for all specimens.

Acknowledgements This work was financially supported by the National Natural Science Foundation of China (No. 41972283) and the Fundamental Research Funds for the Central Universities of Central South University (No. 2022ZZTS0416).

Data Availability The data are available from the corresponding author on reasonable request.

References

- Abdalla HM, Karihaloo BL (2004) A method for constructing the bilinear tension softening diagram of concrete corresponding to its true fracture energy. *Mag Concr Res* 56:597–604. <https://doi.org/10.1680/macr.56.10.597.53679>
- Bahrami B, Ayatollahi MR, Mirzaei AM, Yahya MY (2020) Support Type Influence on Rock Fracture Toughness Measurement Using Semi-circular Bending Specimen. *Rock Mech Rock Eng* 53:2175–2183. <https://doi.org/10.1007/s00603-019-02023-z>
- Blaber J, Adair B, Ncorr AA (2015) Open-Source 2D Digital Image Correlation Matlab Software. *Exp Mech* 55:1105–1122. <https://doi.org/10.1007/s11340-015-0009-1>
- Cen D, Huang D, Song Y, Jiang Q (2020) Direct Tensile Behavior of Limestone and Sandstone with Bedding Planes at Different Strain Rates. *Rock Mech Rock Eng* 53:2643–2651. <https://doi.org/10.1007/s00603-020-02070-x>
- Chen HH, Su R (2013) Tension softening curves of plain concrete. *Constr Build Mater* 44(44):440–451. <https://doi.org/10.1016/j.conbuildmat.2013.03.040>
- Chen YJ, Yin TB, Li XB, Li Q, Yang Z, Li MJ, Wu Y (2021) Experimental investigation on dynamic mechanical behavior and fracture evolution of fissure-filled red sandstone after thermal treatment. *Eng Geol* 295:106433. <https://doi.org/10.1016/j.enggeo.2021.106433>
- Chen X, Tang J, Zhang N, Dai F, Wei M (2022) Fracture analysis of three-point bending notched granite beams under prepeak and postpeak cyclic loading by digital image correlation and acoustic emission techniques. *Fat Fract Eng Mater Struct.* 45(3):904–920. <https://doi.org/10.1111/ffe.13646>
- Dong W, Wu Z, Zhou X (2013) Calculating crack extension resistance of concrete based on a new crack propagation criterion. *Constr Build Mater* 38:879–889. <https://doi.org/10.1016/j.conbuildmat.2012.09.037>
- Dong W, Wu Z, Zhou X, Wang C (2016) A comparative study on two stress intensity factor-based criteria for prediction of mode-I crack propagation in concrete. *Eng Fract Mech* 158:39–58. <https://doi.org/10.1016/j.engfracmech.2018.05.009>
- Dong W, Wu Z, Tang X, Zhou X (2018) A comparative study on stress intensity factor-based criteria for the prediction of mixed mode I-II crack propagation in concrete. *Eng Fract Mech* 197:217–235. <https://doi.org/10.1016/j.engfracmech.2018.05.009>
- Dong W, Song S, Zhang B, Yang D (2019) SIF-based fracture criterion of rock-concrete interface and its application to the prediction of cracking paths in gravity dam. *Eng Fract Mech* 221:106686. <https://doi.org/10.1016/j.engfracmech.2019.106686>
- Dong W, Wu Z, Zhang B, Ji S (2021) Study on shear-softening constitutive law of rock-concrete interface. *Rock Mech Rock Eng* 54:4677–4694. <https://doi.org/10.1007/s00603-021-02536-6>
- Feng G, Kang Y, Meng T, Hu YQ, Li XH (2017) The influence of temperature on mode I fracture toughness and fracture characteristics of sandstone. *Rock Mech Rock Eng* 50:2007–2019. <https://doi.org/10.1007/s00603-017-1226-y>
- Feng P, Zhao J, Dai F, Wei M, Liu B (2022) Mechanical behaviors of conjugate-flawed rocks subjected to coupled static–dynamic compression. *Acta Geotech* 17:1765–1784. <https://doi.org/10.1007/s11440-021-01322-6>
- Gao W, Lin X, Jie H, Feng YT (2022) A novel bilinear constitutive law for cohesive elements to model the fracture of pressure-dependent rocks. *Rock Mech Rock Eng* 55:521–540. <https://doi.org/10.1007/s00603-021-02671-0>
- Ghoulis S, Bahrami B, Ayatollahi MR, Driesner T, Nejati M (2021) Introduction of a scaling factor for fracture toughness measurement of rocks using the semi-circular bend test. *Rock Mech Rock Engng* 54(8):4041–4058. <https://doi.org/10.1007/s00603-021-02468-1>
- Guinea GV, Planas J, Elices M (1994) A general bilinear fit for the softening curve of concrete. *Mater Struct* 27(2):99–105. <https://doi.org/10.1007/bf02472827>
- Hallett SR, Harper PW (2015) 2 - Modelling delamination with cohesive interface elements. In: Camanho PP, Hallett SR (eds) *Woodhead Publishing Series in composites science and engineering, numerical modelling of failure in advanced composite materials*. Woodhead Publishing, USA
- Hillerborg A, Mod er M, Petersson PE (1976) Analysis of crack formation in concrete by means of fracture mechanics and finite elements. *Cem Concr Res* 6:773–781. [https://doi.org/10.1016/0008-8846\(76\)90007-7](https://doi.org/10.1016/0008-8846(76)90007-7)
- Hu S, Fan B (2019) Study on the bilinear softening mode and fracture parameters of concrete in low temperature environments. *Eng Fract Mech* 211:1–16. <https://doi.org/10.1016/j.engfracmech.2019.02.002>
- Jenq YS, Shah SP (1985) A fracture toughness criterion for concrete. *Eng Fract Mech* 21(5):1055–1069. [https://doi.org/10.1016/0013-7944\(85\)90009-8](https://doi.org/10.1016/0013-7944(85)90009-8)
- Jiao K, Han D, Wang D, Chen Y, Li J et al (2022) Investigation of thermal-hydro-mechanical coupled fracture propagation considering rock damage. *Comput Geosci*. <https://doi.org/10.1007/s10596-022-10155-5>
- Jing Z, Wu XR (2015) Wide-range weight functions and stress intensity factors for arbitrarily shaped crack geometries using complex Taylor series expansion method. *Eng Fract Mech* 138:215–232. <https://doi.org/10.1016/j.engfracmech.2015.03.006>
- Karihaloo BL, Nallathambi P (1990) Effective crack model for the determination of fracture toughness (K_{IC}) of concrete. *Eng Fract Mech* 35(4–5):637–645. [https://doi.org/10.1016/0013-7944\(90\)90146-8](https://doi.org/10.1016/0013-7944(90)90146-8)
- Kwon SH, Zhao Z, Shah SP (2008) Effect of specimen size on fracture energy and softening curve of concrete Inverse analysis and softening curve. *Cem Conc Res* 38:1061–1069. <https://doi.org/10.1016/j.cemconres.2008.03.014>
- Lee SK, Woo SK, Song YC (2008) Softening response properties of plain concrete by large-scale direct tension tests. *Mag Concr Res* 60(1):33–40. <https://doi.org/10.1680/macr.2007.00037>
- Li J, Guo Z, Ai D, Yang J, Wei Z (2021) A simplified estimation method for tensile softening curve of quasi-brittle materials. *Mech Adv Mater Struct*. <https://doi.org/10.1080/15376494.2021.1991060>
- Lin Q, Wang S, Pan P-Z, Bian X, Lu Y (2020) Imaging opening-mode fracture in sandstone under three-point bending: A direct identification of the fracture process zone and traction-free crack based on cohesive zone model. *Int J Rock Mech Min Sci* 136:104516. <https://doi.org/10.1016/j.ijrmms.2020.104516>
- Liu S, Xu J (2015) An experimental study on the physico-mechanical properties of two post-high-temperature rocks. *Eng Geol* 185:63–70
- Mai YW (2002) Cohesive zone and crack-resistance (R)-curve of cementitious materials and their fibre-reinforced composites. *Eng Fract Mech* 69:219–234. [https://doi.org/10.1016/S0013-7944\(01\)00086-8](https://doi.org/10.1016/S0013-7944(01)00086-8)
- Mardoukhi A, Mardoukhi Y, Hokka M, Kuokkala VT (2017) Effects of Heat Shock on the Dynamic Tensile Behavior of Granitic Rocks.

- Rock Mech Rock Eng 50:1171–1182. <https://doi.org/10.1007/s00603-017-1168-4>
- Meredith PG, Atkinson BK (1985) Fracture toughness and subcritical crack growth during high-temperature tensile deformation of Westerly granite and Black gabbro. *Phys Earth Planet Inter* 39(1):33–51. [https://doi.org/10.1016/0031-9201\(85\)90113-X](https://doi.org/10.1016/0031-9201(85)90113-X)
- Miao S, Pan P-Z, Yu P, Zhao S, Shao C (2020) Fracture analysis of Beishan granite after high-temperature treatment using digital image correlation. *Eng Fract Mech* 225:106847. <https://doi.org/10.1016/j.engfracmech.2019.106847>
- Murthy AR, Karihaloo BL, Iyer NR, Prasad BK (2013) Bilinear tension softening diagrams of concrete mixes corresponding to their size-independent specific fracture energy. *Constr Build Mater* 47:1160–1166. <https://doi.org/10.1016/j.conbuildmat.2013.06.004>
- Nasseri M, Schubnel A, Young RP (2007) Coupled evolutions of fracture toughness and elastic wave velocities at high crack density in thermally treated Westerly granite. *Int J Rock Mech Min Sci* 44(4):601–616. <https://doi.org/10.1016/j.ijrmmms.2006.09.008>
- Rasmussen LL, De Farias MM, De Assis AP (2018) Extended rigid body spring network method for the simulation of brittle rocks. *Comp Geotech* 99:31–41. <https://doi.org/10.1016/j.compgeo.2018.02.021>
- Reinhardt HW, Xu S (1999) Crack extension resistance based on the cohesive force in concrete. *Eng Fract Mech* 64:563–587. [https://doi.org/10.1016/S0013-7944\(99\)00080-6](https://doi.org/10.1016/S0013-7944(99)00080-6)
- Reinhardt HW, Cornelissen H, Hordijk DA (1986) Tensile tests and failure analysis of concrete. *J Struct Eng* 112(11):2462–2477. [https://doi.org/10.1061/\(ASCE\)0733-9445\(1986\)112:11\(2462\)](https://doi.org/10.1061/(ASCE)0733-9445(1986)112:11(2462))
- Sciarretta F, Sciarretta EJ, Beaucour AL (2021) State-of-the-art of construction stones for masonry exposed to high temperatures. *Construct Build Mater*. 304:124536. <https://doi.org/10.1016/j.conbuildmat.2021.124536>
- Shao Z, Sun L, Aboyanah KR, Liu Q, Grasselli G (2022) Investigate the mode I fracture characteristics of granite after heating/–ln2 cooling treatments. *Rock Mech Rock Eng* 55:4477–4496. <https://doi.org/10.1007/s00603-022-02893-w>
- Shen G, Glinka G (1991) Determination of weight functions from reference stress intensity factors. *Theoret Appl Fract Mech* 15:237–245. [https://doi.org/10.1016/0167-8442\(91\)90022-C](https://doi.org/10.1016/0167-8442(91)90022-C)
- Shet C, Chandra N (2004) Effect of the Shape of T– δ Cohesive Zone Curves on the Fracture Response. *Mech Adv Mater Struct* 11(3):249–275. <https://doi.org/10.1080/15376490490427207>
- Sirdesai NN, Singh TN, Ranjith PG, Singh R (2017) Effect of Varied Durations of Thermal Treatment on the Tensile Strength of Red Sandstone. *Rock Mech Rock Eng* 50:205–213. <https://doi.org/10.1007/s00603-016-1047-4>
- Slowik V, Villmann B, Bretschneider N, Villmann T (2006) Computational aspects of inverse analyses for determining softening curves of concrete. *Comput Methods Appl Mech Eng* 195(52):7223–7236. <https://doi.org/10.1016/j.cma.2005.04.021>
- Tada H, Paris PC, Irwin G (2000) *The stress analysis of cracks handbook*, 3rd edn. ASME Press, New York. <https://doi.org/10.1115/1.801535>
- Tang Y, Chen H, Xiao J (2022) Size effects on the characteristics of fracture process zone of plain concrete under three-point bending. *Construct Build Mater*. 315:125725. <https://doi.org/10.1016/j.conbuildmat.2021.125725>
- Ulfkjaer JP, Krenk S, Brincker R (1995) Analytical model for fictitious crack propagation in concrete beams. *J Eng Mech*. [https://doi.org/10.1061/\(ASCE\)0733-9399\(1995\)121:1\(7\)](https://doi.org/10.1061/(ASCE)0733-9399(1995)121:1(7))
- Wang HW, Wu ZM, Wang YJ (2019) Yu RC (2019) An analytical method for predicting mode-I crack propagation process and resistance curve of rock and concrete materials. *Theoret Appl Fract Mech* 100:328–341. <https://doi.org/10.1016/j.tafmec.2019.01.019>
- Wei MD, Dai F, Xu N, Zhao T, Xia K (2016) Experimental and numerical study on the fracture process zone and fracture toughness determination for ISRM-suggested semi-circular bend rock specimen. *Eng Fract Mech* 154:43–56. <https://doi.org/10.1016/j.engfracmech.2016.01.002>
- Wei MD, Dai F, Liu Y, Li A, Yan Z (2021) Influences of Loading Method and Notch Type on Rock Fracture Toughness Measurements. *Perspect T-Stress Fract Zone*. 54:4965–4986
- Wei MD, Dai F, Liu Y, Jiang R (2022) A fracture model for assessing tensile mode crack growth resistance of rocks. *J Rock Mech Geotech Eng* 15(2):395–411. <https://doi.org/10.1016/j.jrmge.2022.03.001>
- Wu ZM, Hua R, Zheng JJ, Feng X, Wei D (2011) An experimental investigation on the FPZ properties in concrete using digital image correlation technique. *Eng Fract Mech* 78:2978–2990. <https://doi.org/10.1016/j.engfracmech.2011.08.016>
- Wu Z, Wu Y, Wu X, Dong W, Zheng J (2014) An analytical method for determining the crack extension resistance curve of concrete. *Mag Concr Res* 66(4):719–728. <https://doi.org/10.1680/macr.13.00228>
- Wu XR, Tong DH, Zhao XC, Xu W (2018a) Review and evaluation of weight functions and stress intensity factors for edge-cracked finite-width plate. *Eng Fract Mech* 195:200–221. <https://doi.org/10.1016/j.engfracmech.2018.04.001>
- Wu Z, Ma L, Fan L (2018b) Investigation of the characteristics of rock fracture process zone using coupled FEM/DEM method. *Eng Fract Mech* 200:355–374. <https://doi.org/10.1016/j.engfracmech.2018.08.015>
- Wu Z, Zhang P, Fan L, Liu Q (2019) Numerical study of the effect of confining pressure on the rock breakage efficiency and fragment size distribution of a TBM cutter using a coupled FEM-DEM method. *Tunn Underground Space Technol* 88:260–275. <https://doi.org/10.1016/j.tust.2019.03.012>
- Wu Y, Yin T, Tan X, Zhuang D (2021) Determination of the mixed mode I/II fracture characteristics of heat-treated granite specimens based on the extended finite element method. *Eng Fract Mech* 252:107818. <https://doi.org/10.1016/j.engfracmech.2021.107818>
- Wu D, Yu L, Ju M, Li S, Liu R, Su H, Zhou L (2022a) Study on the mode I fracture properties of granites after heating and water-cooling treatments under different impact loadings. *Rock Mech Rock Eng* 55:4271–4290. <https://doi.org/10.1007/s00603-022-02865-0>
- Wu Y, Yin TB, Zhuang DD, Li Q, Chen YJ (2022b) Research on the effect of thermal treatment on the crack resistance curve of marble using notched semi-circular bend specimen. *Theoret Appl Fract Mech* 119:103344. <https://doi.org/10.1016/j.tafmec.2022.103344>
- Wu Y, Yin T, Li Q, Zhuang D, Chen Y, Yang Z (2022c) Analytical investigation on the unstable fracture toughness of fine-grained quartz-diorite rock considering the size effect. *Eng Fract Mech* 272:108722. <https://doi.org/10.1016/j.engfracmech.2022.108722>
- Xu S, Reinhardt HW (1999) Determination of double-K criterion for crack propagation in quasi-brittle materials, Part I. *Int J Fract* 98(2):111–193
- Xu Y, Yao W, Wang S, Xia K (2020) Investigation of the heat-treatment effect on rock fragmentation characteristics using the dynamic ball compression test. *Rock Mech Rock Eng* 53(5):2095–2108. <https://doi.org/10.1007/s00603-019-02038-6>
- Yan Z, Dai F, Liu Y, Wei M, You W (2021) New insights into the fracture mechanism of flattened Brazilian disc specimen using digital image correlation. *Eng Fract Mech* 252:107810. <https://doi.org/10.1016/j.engfracmech.2021.107810>
- Yang G, Cai Z, Zhang X, Fu D (2015) An experimental investigation on the damage of granite under uniaxial tension by using a digital image correlation method. *Opt Lasers Eng* 73:46–52. <https://doi.org/10.1016/j.optlaseng.2015.04.004>
- Yang SQ, Ranjith PG, Jing HW, Tian WL, Ju Y (2017) An experimental investigation on thermal damage and failure mechanical behavior of granite after exposure to different high temperature

- treatments. *Geothermics* 65:180–197. <https://doi.org/10.1016/j.geothermics.2016.09.008>
- Yang Z, Yin TB, Zhuang D, Wu Y, Yin J, Chen Y (2022) Effect of temperature on mixed mode fracture behavior of diorite: An experimental investigation. *Theoret Appl Fract Mech* 122:103571. <https://doi.org/10.1016/j.tafmec.2022.103571>
- Ye Y, Ma J, Wu Z, Zeng Y (2021) A novel 3D-FDEM method using finite-thickness cohesive elements to simulate the nonlinear mechanical behaviors of rocks. *Comp Geotech.* 140:104478. <https://doi.org/10.1016/j.compgeo.2021.104478>
- Yin TB, Li XB, Cao WZ, Xia KW (2015) Effects of thermal treatment on tensile strength of laurentian granite using brazilian test. *Rock Mech Rock Eng* 48(6):2213–2223. <https://doi.org/10.1007/s00603-015-0712-3>
- Yin TB, Li Q, Li XB (2019) Experimental investigation on mode I fracture characteristics of granite after cyclic heating and cooling treatments. *Eng Fract Mech* 222:106740. <https://doi.org/10.1016/j.engfracmech.2019.106740>
- Yin TB, Zhuang DD, Li Q, Tan XS, Wu Y (2021) Effect of oxygen on damage mechanism and mechanical properties of sandstone at high temperature. *Bull Eng Geol Env* 80(8):6047–6064. <https://doi.org/10.1007/s10064-021-02317-z>
- Yin TB, Yang Z, Wu Y, Tan XS, Li MJ (2022) Experimental investigation on the effect of open fire on the tensile properties and damage evolution behavior of granite. *Int J Damage Mech* 31(8):1139–1164. <https://doi.org/10.1177/10567895221092168>
- Yin X, Li Q, Wang Q, Reinhardt HW, Xu S (2023) The double-K fracture model A state-of-the-art review. *Eng Fract Mech* 277:108988. <https://doi.org/10.1016/j.engfracmech.2022.108988>
- Zhang ZX, Ouchterlony F (2022) Energy requirement for rock breakage in laboratory experiments and engineering operations: a review. *Rock Mech Rock Eng* 55:629–667. <https://doi.org/10.1007/s00603-021-02687-6>
- Zhang J, Leung C, Xu S (2010) Evaluation of fracture parameters of concrete from bending test using inverse analysis approach. *Mater Struct* 43(6):857–874. <https://doi.org/10.1617/s11527-009-9552-5>
- Zhang Y, Ta X, Qin S (2022a) Effect of heat treatment on physico-mechanical behaviour of a natural building stone: Laizhou dolomite marble. *J Build Eng* 45:103885. <https://doi.org/10.1016/j.job.2021.103885>
- Zhang D, Meng T, Taherdangkoo R, Feng G, Wen L, Butscher C (2022b) Evolution trend and weakening mechanism of mode-I fracture characteristics of granite under coupled thermo-hydro-mechanical and thermal treatments. *Eng Fract Mech* 275:108794. <https://doi.org/10.1016/j.engfracmech.2022.108794>
- Zhao G, Yao W, Li X, Xu Y, Xia K, Chen R (2022) Influence of notch geometry on the rock fracture toughness measurement using the isrm suggested semi-circular bend (SCB) method. *Rock Mech Rock Eng* 55:2239–2253. <https://doi.org/10.1007/s00603-022-02773-3>
- Zhu QQ, Li CJ, Li XB, Li DY, Wang WH, Chen JZ (2022a) Fracture mechanism and energy evolution of sandstone with a circular inclusion. *Int J Rock Mech Min Sci* 155:105139. <https://doi.org/10.1016/j.ijrmms.2022.105139>
- Zhu J, Deng J, Chen F, Wang F (2022b) Failure analysis of water-bearing rock under direct tension using acoustic emission. *Eng Geol* 299:106541. <https://doi.org/10.1016/j.enggeo.2022.106541>
- Zhuang DD, Yin T, Li Q, Wu Y, Chen Y, Yang Z (2022) Fractal fracture toughness measurements of heat-treated granite using hydraulic fracturing under different injection flow rates. *Theoret Appl Fract Mech* 119:103340. <https://doi.org/10.1016/j.tafmec.2022.103340>

Publisher's Note Springer Nature remains neutral with regard to jurisdictional claims in published maps and institutional affiliations.

Springer Nature or its licensor (e.g. a society or other partner) holds exclusive rights to this article under a publishing agreement with the author(s) or other rightsholder(s); author self-archiving of the accepted manuscript version of this article is solely governed by the terms of such publishing agreement and applicable law.